

The APOGEE Library of Infrared SSP Templates (A-LIST): High-resolution Simple Stellar Population Spectral Models in the H Band

Aishwarya Ashok¹, Gail Zasowski¹, Anil Seth¹, Sten Hasselquist^{1,9}, Galen Bergsten¹, Olivia Cooper², Nicholas Boardman¹, Dmitry Bizyaev^{3,4}, Sofia Meneses Goytia⁵, D. A. García-Hernández^{6,7}, and Alexandre Roman-Lopes⁸ Department of Physics and Astronomy, University of Utah, Salt Lake City, UT 84112, USA ² Department of Astronomy, The University of Texas at Austin, 2515 Speedway Boulevard Stop C1400, Austin, TX 78712, USA Apache Point Observatory and New Mexico State University, P.O. Box 59, Sunspot, NM, 88349-0059, USA Sternberg Astronomical Institute, Moscow State University, Moscow, Russia ⁵ Department of Physics, Astrophysics Research Group, University of Surrey, Guildford, Surrey, GU2 7X, UK Instituto de Astrofísica de Canarias (IAC), E-38205 La Laguna, Tenerife, Spain ⁷ Universidad de La Laguna (ULL), Departamento de Astrofísica, E-38206, La Laguna, Tenerife, Spain ⁸ Departamento de Física, Facultad de Ciencias, Universidad de La Serena, Cisternas 1200, La Serena, Chile Received 2020 July 17; revised 2020 December 29; accepted 2020 December 31; published 2021 March 8

Abstract

Integrated light spectroscopy from galaxies can be used to study the stellar populations that cannot be resolved into individual stars. This analysis relies on stellar population synthesis (SPS) techniques to study the formation history and structure of galaxies. However, the spectral templates available for SPS are limited, especially in the nearinfrared (near-IR). We present A-LIST (APOGEE Library of Infrared SSP Templates), a new set of highresolution, near-IR SSP spectral templates spanning a wide range of ages (2–12 Gyr), metallicities (-2.2 < M) H] < + 0.4) and α abundances (-0.2 < $[\alpha/M]$ < + 0.4). This set of SSP templates is the highest resolution $(R \sim 22, 500)$ available in the near-IR, and the first such based on an empirical stellar library. Our models are generated using spectra of $\sim 300,000$ stars spread across the Milky Way, with a wide range of metallicities and abundances, from the APOGEE survey. We show that our model spectra provide accurate fits to M31 globular cluster spectra taken with APOGEE, with best-fit metallicities agreeing with those of previous estimates to within ~0.1 dex. We also compare these model spectra to lower-resolution E-MILES models and demonstrate that we recover the ages of these models to within ~ 1.5 Gyr. This library is available in https://github.com/aishashok/ ALIST-library.

Unified Astronomy Thesaurus concepts: Galaxy stellar content (621); Galaxy chemical evolution (580); Stellar evolutionary models (2046); Stellar evolution (1599)

1. Introduction

Observing, modeling, and analysis of individual stars in the visible spectrum have formed the foundation for our understanding of stellar evolution. In turn, our understanding of galaxies today—their star formation rates, evolutionary histories, and stellar masses—is almost entirely based on our knowledge of stellar evolution. Resolved stellar populations allow us to measure the colors, luminosities, and compositions of individual stars and provides useful information about the history and structure of their galaxies. Resolved population studies are possible only in the Milky Way (e.g., Ruiz-Lara et al. 2020) as well as nearby spiral and dwarf galaxies (e.g., Williams et al. 2009; Weisz et al. 2011; Lewis et al. 2015). In more distant galaxies, integrated spectroscopy has been an important method to study their unresolved stellar content. The integrated spectrum of a population reflects its star formation histories and chemical enrichment. Using spectral lines to study the physical properties of stars and stellar populations has been known as early as 1960s and has improved ever since (Spinrad & Taylor 1971; Mould 1978; Chavez et al. 1996; Parikh et al. 2019).

Earlier work studying galaxy stellar populations focused primarily on line index measurements (e.g., Worthey et al. 1994; Trager et al. 2000; Thomas et al. 2003; Gallazzi et al.

2005; Schiavon 2007; Caldwell et al. 2011) in the optical part

of the spectrum as well as in the near-infrared (NIR; e.g., Vazdekis et al. 1996; Böker et al. 1999; Cenarro et al. 2001;

Förster Schreiber et al. 2003; Cenarro et al. 2009; MacArthur

et al. 2010; Vazdekis et al. 2010; Onken et al. 2014; Riffel et al.

2019). In recent years, full spectral fitting of integrated light

spectra to model spectra has opened a new window to study in

detail the physical, chemical, and evolutionary phases of galaxy

stellar populations (e.g., Pérez et al. 2013; Pace et al. 2019;

Boardman et al. 2020). Some of the most widely used spectral

fitting software for this technique are FIREFLY (Wilkinson

et al. 2017), STECKMAP (Ocvirk et al. 2006), VESPA

(Tojeiro 2007), the penalized pixel-fitting method (pPXF;

Cappellari et al. 2009), ULySS (Koleva et al. 2009), STAR-

LIGHT (Cid Fernandes et al. 2011), and Pipe3D (Sánchez et al.

2016a, 2016b). Most of the pixel-fitting stellar population

studies to date have used optical spectroscopy to derive

information about galaxy formation histories (e.g., Heavens

et al. 2004; McDermid et al. 2015). The NIR part of the

spectrum offers some advantages over the optical due to the

reduced effects of dust extinction and the sensitivity to cool

stars. Over the past decade or so, a large number of studies

have studied stellar populations using the NIR (e.g., Silva et al.

2008; Cesetti et al. 2009; Mármol-Queraltó et al. 2008; Sakari

et al. 2016; La Barbera et al. 2016, 2017; Röck et al. 2017;

Baldwin et al. 2018; Dahmer-Hahn et al. 2018; Martins et al. 2019; Coelho et al. 2020). These direct spectral fitting techniques use the stellar population synthesis (SPS) technique, where spectra are modeled

⁹ NSF Postdoctoral Fellow.

with a combination of synthetic populations to disentangle their age and chemical abundances. The foundation of this method is the simple stellar population (SSP) model, where all stars are coeval and share the same chemical composition. Creating model stellar populations has progressed greatly in the last three decades from the trial-and-error technique (e.g., Tinsley 1968; Bruzual & Charlot 2003; Maraston 2005; Vazdekis et al. 2010; Röck et al. 2016; Conroy et al. 2018).

Given the wide range of information we want to gain from SPS fitting—the star formation history and rate, initial mass function (IMF), chemical enrichment, metallicity, etc.—creating optimal and flexible SSP models remains a major challenge in modern evolutionary studies. There are two ways these SSPs can be constructed: (i) fuel-consumption-based approach (e.g., Maraston 2005) and (ii) the isochrone synthesis approach, which we use in this paper. With the isochrone synthesis method, we can construct the SSPs as having an IMF along an isochrone and a stellar library (e.g., Bruzual & Charlot 2003).

The theoretical stellar libraries (e.g., MARCS library; Gustafsson et al. 2008) are generated using a desired range of parameters that cannot be obtained from observations at any range of wavelength, while the empirical libraries (e.g., ELODIE library, X-shooter Library ($R \sim 10,000$); Prugniel et al. 2007; Gonneau et al. 2020) are based on real observational data. Large spectroscopic surveys like APOGEE (Majewski et al. 2017), GALAH (De Silva et al. 2015), etc. can provide us with tens of thousands of Milky Way star properties that can be used to model stellar populations. To study the stellar absorption features in old populations, empirical libraries are preferred (Maraston et al. 2009; Vazdekis et al. 2016), while for young and bright populations, theoretical libraries are preferred (Maraston 2005; Leitherer et al. 2014). Martins et al. (2019) and Coelho et al. (2020) explain in detail how these two types of libraries are used.

The models we present here address two specific deficits in existing SPS models. First, most models do not consider varying α abundances, and α abundances are typically still derived using spectral indices rather than pixel fitting to SPS models (e.g., Schiavon et al. 2012; Janz et al. 2016; Johnston et al. 2020). Second, there are no SPS models based on empirical stellar libraries in the NIR available at high spectral resolution. The only high-spectral-resolution NIR models $(R \sim 20,000)$ are the version of the Maraston & Strömbäck (2011) models created using the MARCS theoretical stellar spectra library. See Baldwin et al. (2018) for how these models compare with other available NIR models and data. Existing models based on empirical stellar libraries available in the NIR (Bruzual & Charlot 2003; Maraston & Strömbäck 2011; Meneses-Goytia et al. 2015; Vazdekis et al. 2016; Röck et al. 2016; Conroy et al. 2018) use the Pickles (1998) stellar library and the IRTF library (Cushing et al. 2005; Rayner et al. 2009). Both of these have low spectral resolution, with the IRTF library having the higher resolution of $R \sim 2000$.

This spectral resolution is lower than that of many current and planned spectrographs: Gemini/NIFS (McGregor et al. 2003), VLT/SINFONI (Eisenhauer et al. 2003), GEMINI/GNIRS (Elias et al. 2006), ESO/KMOS (Wisnioski et al. 2015), VLT/MOONS (Cirasuolo 2016), Keck/MOSFIRE (Steidel et al. 2014), and JWST/NIRSPEC (Ygouf et al. 2017). For data taken from these spectrographs, using the current available models based on empirical stellar libraries requires degrading the data resolution and losing information while modeling.

In this paper, we present A-LIST (APOGEE Library of Infrared SSP Templates), a new library of high-resolution SSP spectral models generated using a new empirical stellar library based on Apache Point Observatory Galaxy Evolution Experiment (APOGEE; Majewski et al. 2017) data from the Sloan Digital Sky Survey IV (SDSS-IV; Blanton et al. 2017). The SSP models range in age, [M/H] and $[\alpha/M]$. This is a first-ofits-kind spectral library in the H-band region having a high spectral resolution ($R \sim 22,500$). This library can be used to model, for example, (i) any near-IR integrated light spectra having a spectral resolution greater than the current available SSP models, (ii) α enhancement and kinematics of globular clusters (GCs) and/or early-type galaxies, and (iii) nearby galaxy data (M31, M33) available from APOGEE (Zasowski et al. 2013; R. L. Beaton et al. 2021, in preparation). Because APOGEE spectra are not precisely flux calibrated, A-LIST spectral models are primarily useful for integrated light spectroscopic studies.

We discuss the required ingredients and our selections in Section 2. In Section 3, we discuss how we generate the SSP models in detail. In Section 4, we present our spectral models. In Section 5, we present our validation of these models by reproducing properties of M31 GCs and comparisons to previously studied models. The summary along with future work is described in Section 6.

2. Simple Stellar Population Model Ingredients

In this section, we outline the main ingredients, including the isochrone sets (Section 2.1) and the stellar library (Section 2.2).

2.1. Stellar Evolution and Isochrones

One of the main ingredients to generate an SSP model is an isochrone or a set of stellar evolutionary tracks.

For our models, we use two different isochrone sets:

- 1. PARSEC isochrones: the latest Padova isochrones and stellar evolutionary tracks (Bressan et al. 2012; Chen et al. 2014, 2015; Tang et al. 2014; Marigo et al. 2017; Pastorelli et al. 2019) are computed spanning a wide range in ages and metallicities. The library of isochrones includes stars with initial masses $M = 0.15-100~M_{\odot}$, $\log(\text{age}) = 6.6-10.2$, and metallicities [M/H] = -2.2 +0.5. The PARSEC stellar tracks range in initial metal content (z_i) from 0.0001 to 0.06, with 15 values in the grid, and range in mass from 0.1 to 350 M_{\odot} with \sim 120 different mass values for each metallicity (Marigo et al. 2017).
- 2. MIST evolutionary tracks: MESA Isochrones and Stellar Tracks (MIST; Dotter 2016; Choi et al. 2016; Paxton et al. 2011, 2013, 2015) is another set of evolutionary track models thas an extensive range of mass $(M=0.1-300~M_\odot)$, age $(\log(age)=5-10.3)$, and metallicity $(-4\leqslant [\mathrm{M/H}]\leqslant +0.5)$. The evolutionary tracks used to generate the isochrones range in mass from 0.1 to 300 M_\odot with >100 models at different masses, and in [Fe/H] from -2.0 to +0.5 with 0.25 dex spacing (Choi et al. 2016). We use the models with $v/v_{\mathrm{crit}}=0.0$, i.e., those models that do not include any stellar rotation parameters in them.

Both sets of models use interpolation of the evolutionary tracks to create isochrones at a given age and metallicity. The list of ages and metallicities used in our models is given in Section 4.

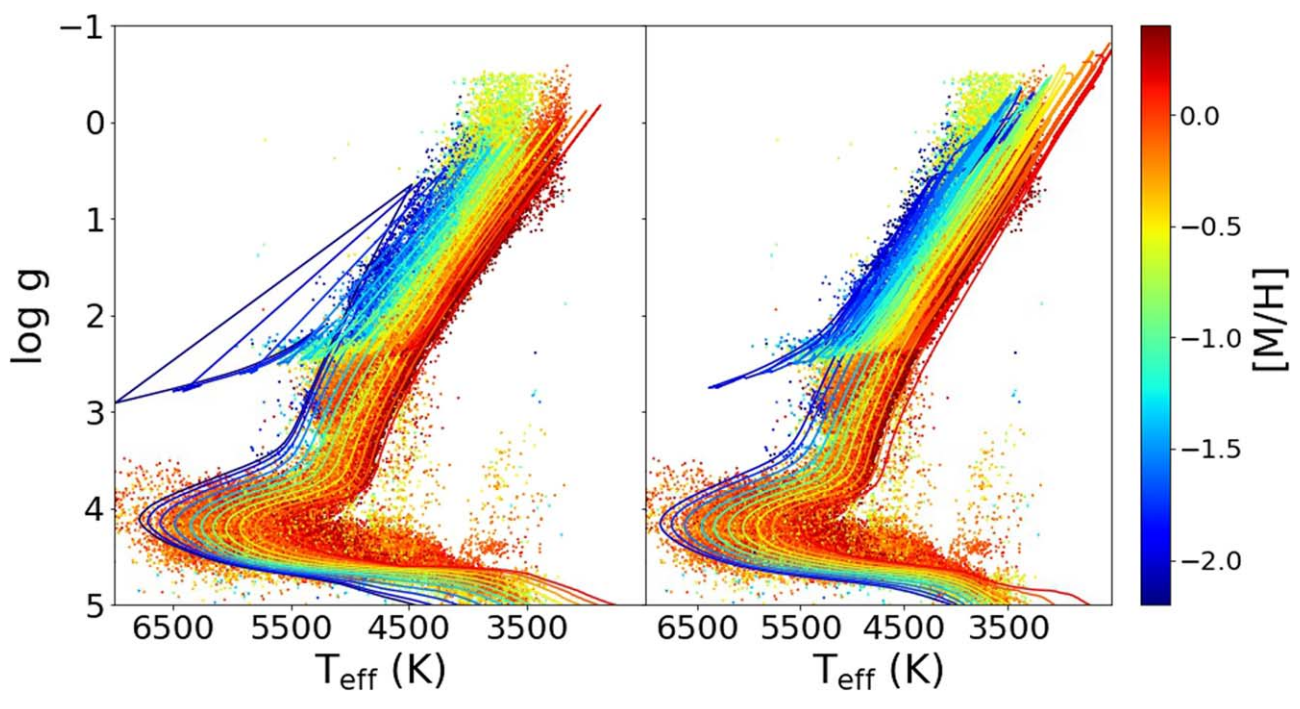


Figure 1. Isochrones (lines) plotted over the empirical library of APOGEE stars (points). Both are colored by their metallicity. The isochrones plotted are for a 10 Gyr and solar $[\alpha/M]$ population. The left panel shows the Padova isochrones, and the right panel shows the same for the MIST isochrones.

One of the main differences between the PARSEC and the MIST isochrones is the method used to interpolate the thermal pulsating asymptotic giant branch (TP-AGB) evolutionary tracks. This results in the C-rich AGB stars in the MIST isochrones starting at a later point in their evolutionary track compared to those of PARSEC (Choi et al. 2016; Marigo et al. 2017). The C-rich AGB stars in MIST isochrones are hotter than those in PARSEC mainly because the MIST isochrones use molecular opacities derived for O-rich mixtures (Marigo et al. 2017). For a detailed description of how these two isochrone sets differ, see Choi et al. (2016), Marigo et al. (2017), and Cignoni et al. (2019).

Figure 1 shows the two isochrone sets plotted over the empirical library of APOGEE stars (Section 2.2) colored by metallicity, with Padova isochrones on the left and MIST on the right.

The isochrones available in Padova and MIST have solar α abundances. To obtain the most accurate isochrones for our models with nonsolar α abundance ($[\alpha/M]$), we use the α -enhanced metallicity equation (from Salaris & Cassisi 2005, ch. 8) for the solar-scaled isochrones with the metallicity as

$$[M/H]_{iso} = [M/H] + log(0.694 \times 10^{[\alpha/M]} + 0.306),$$
 (1)

where [M/H] is the solar-scaled metallicity and [M/H]_{iso} gives the effective metallicity of the isochrones used to account for the α enhancement. We note that we use this [M/H]_{iso} value only for selecting the isochrones of appropriate metallicity for a model with desired [α /M] and solar-scaled [M/H].

2.2. Empirical Stellar Library

The second main ingredient needed to generate an SSP model is the empirical stellar spectral library. One strength of A-LIST is the availability of several hundred thousand stellar spectra from the APOGEE survey that can be used as an empirical library. APOGEE (Majewski et al. 2017) is a

spectroscopic survey of the Milky Way and a component of the Sloan Digital Sky Survey (SDSS-III and -IV; Eisenstein et al. 2011; Blanton et al. 2017)

APOGEE samples stars that span across the Milky Way's bulge, disk, and halo with a wide range of stellar parameters and abundances (Zasowski et al. 2017, 2013). The data are collected with two 300-fiber spectrographs (Wilson et al. 2019) at the 2.5 m Sloan Foundation Telescope at the Apache Point Observatory in New Mexico (Gunn et al. 2006) and at the 2.5 m duPont Telescope at Las Campanas Observatory in Chile (Bowen & Vaughan 1973). The wavelength range of APOGEE spectra is 1.51–1.70 μ m, which is divided across three chips: the "blue" chip at 1.51–1.581 μ m, "green" chip at $1.585-1.644 \mu m$, and "red" chip at $1.647-1.700 \mu m$, with gaps between the detectors at 1.581–1.585 μ m and 1.644–1.647 μ m). APOGEE's average resolving power (R) is \sim 22,500 based on a direct-measured FWHM of ~ 0.7 Å, with 10%–20% variations seen across the wavelength and fiber (see Section 6.2 of Nidever et al. 2015).

We use an internal APOGEE data release that is an increment from the latest public data release (DR16; Ahumada et al. 2020), which has new stars added from the observing period through 2019 November. The incremental release applies the same DR16 pipeline (Jönsson et al. 2020) to the additional data, which include both new targets and repeat visits for stars in DR16.

APOGEE data are first processed by the APOGEE data reduction pipeline (Nidever et al. 2015). The stellar parameters and elemental abundances are computed by the APOGEE Stellar Parameters and Chemical Abundances Pipeline (ASP-CAP; García Pérez et al. 2016). For our empirical library, we use the calibrated ASPCAP parameters to select cool dwarfs and giants, and the uncalibrated parameters ("FPARAM") to select hot dwarfs ($T_{\rm eff} \ge 7000$ K). See Jönsson et al. (2020) and Holtzman et al. (2018) for a description of APOGEE's calibration procedures and data products.

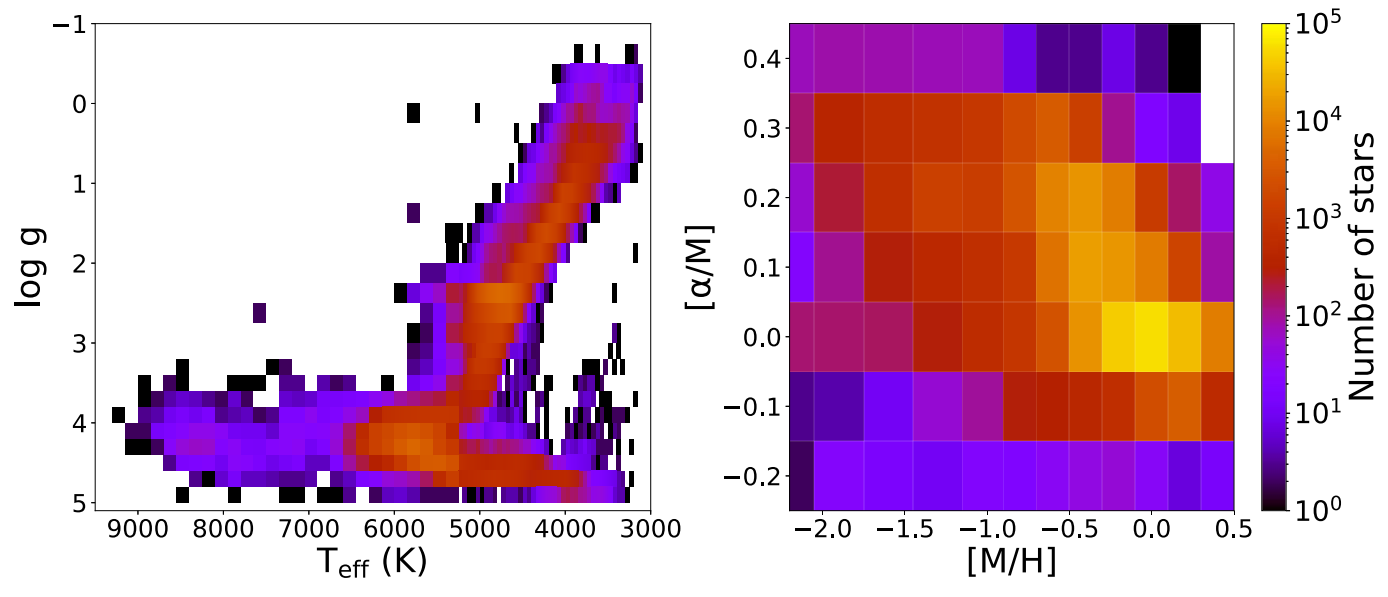


Figure 2. The empirical APOGEE stellar library used to generate our SSP spectral models. The left panel shows an H-R diagram with the number of APOGEE stars selected per $T_{\rm eff}$ and surface gravity bin. The right panel shows the number of selected APOGEE stars in [M/H] and [α /M] space. These bins are defined in Section 3.2.

To obtain a set of APOGEE stars with reliable ASPCAP measurements and high signal-to-noise ratio (S/N), we make the following cuts:

1. S/N: We remove all stars with median S/N per pixel < 100.

When creating the median spectrum for a given stellar parameter bin (Section 3.2), we only consider pixels with an individual $S/N \geqslant 150$, computed with the stellar error spectra.

- 2. VSCATTER: We remove all stars that have a radial velocity scatter greater than 1.5 km s⁻¹. This cut reduces the impact of spectroscopic binary stars on our sample.
- 3. VERR: We remove all stars that have a radial velocity error greater than 3 km s⁻¹. This limit ensures that the selected stars are properly corrected to the rest frame.
- 4. ASPCAPFLAG bitmask: We remove all stars that are marked as STAR_BAD (bit 23), TEFF_BAD (bit 16), LOGG_BAD (bit 17), or COLORTE_WARN (bit 9).
- 5. STARFLAG bitmask: We remove all stars that are marked BRIGHT_NEIGHBOR (bit 2), VERY_BRIGHT_NEIGHBOR (bit 3), PERSIST_HIGH (bit 9), PERSIST_MED (bit 10), PERSIST_LOW (bit 11), SUSPECT_RV_COMBINATION (bit 16), or SUSPECT_BROAD_LINES (bit 17).

Based on these cuts, we select 293,220 stars from the incremental DR16 data. In this paper, we use [M/H] as our solar-scaled metallicity based on its definition in Section 6.5.1 of Majewski et al. (2017). The left panel of Figure 2 shows an H-R diagram of the APOGEE stellar sample that we use as our empirical stellar library. The right panel of Figure 2 shows the [M/H] and [α /M] distribution of the APOGEE stars. Both plots are colored by the number of stars in each bin. The axes on these two plots define the limits within which our models are generated.

We found it necessary to renormalize some of the pseudocontinuum-normalized APOGEE spectra, due to systematic offsets in the pseudo-continuum determination, before combining the spectra. For all stars whose median-normalized flux is greater than 1.04 and stars that show wing-like features (especially at the chip edges), we renormalize the spectra by fitting a third-, fourth-, and third-order polynomial to the blue, green, and red chips of the spectra, respectively. An example of this is shown in Figure 3. Here, the blue line shows the APOGEE pseudo-continuum-normalized spectrum. We see wide wing-like features, most prominently here at the edges of the blue and green detectors. With renormalization, we bring the median flux of the spectrum closer to 1 (as shown in orange).

2.3. Other Data Used in This Paper

Additional data adopted in this paper include stellar ages, used for calculating $\log g$ offsets between the isochrones and the APOGEE stars (Section 3.3). We use ages ('AGE_LOWESS') from the astroNN Value Added Catalog (Leung & Bovy 2019; Mackereth et al. 2019)¹⁰, derived using a neural network trained on the stellar spectra from DR14 (Jönsson et al. 2018).

We also use a set of M31 GC spectra, which were observed as part of an APOGEE ancillary project (Zasowski et al. 2013) as well as a custom analysis of these data performed by Sakari et al. (2016), for validation of our models (Section 5.2). These spectra were made using the APOGEE apVisit files, with an approach nearly identical to the automated APOGEE pipeline that produces the combined apStar files. ¹¹ The difference is that we did not use the measured visit-level radial velocities (RVs) when combining the visit spectra, because we found that some of these RVs were discrepant from the cluster mean; our

¹⁰ https://www.sdss.org/dr16/data_access/value-added-catalogs/?vac_id=the-astronn-catalog-of-abundances,-distances,-and-ages-for-apogee-dr16-stars

¹¹ https://www.sdss.org/dr16/irspec/spectral_combination/

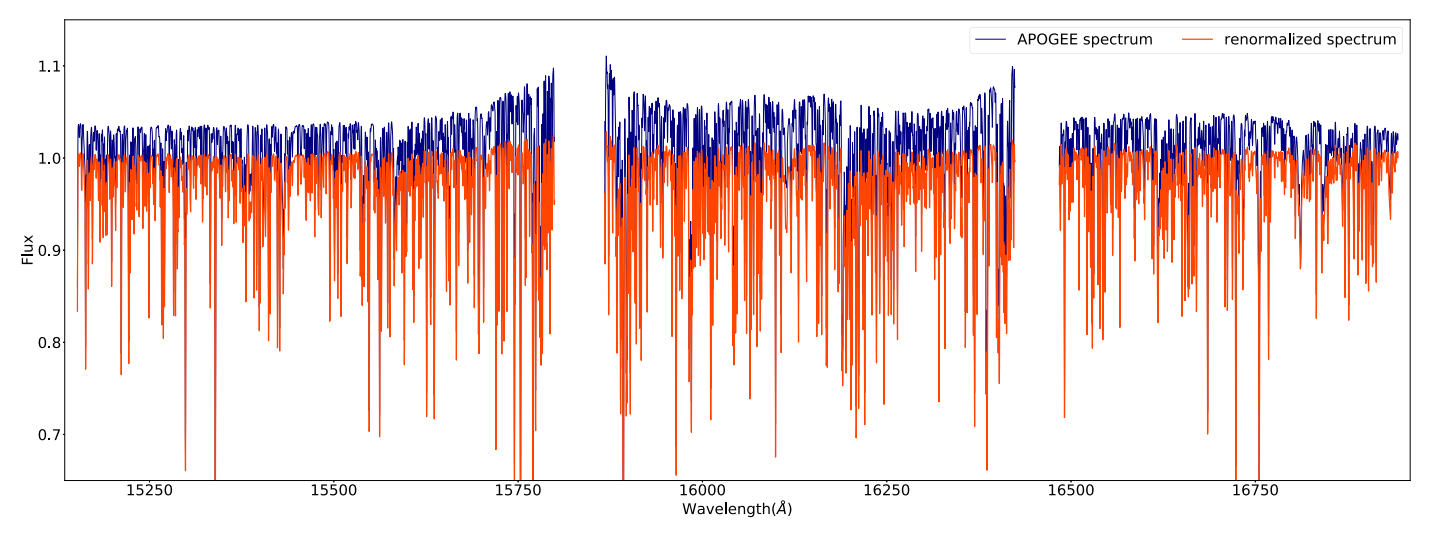


Figure 3. Example of the renormalization of a stellar spectrum. Blue denotes the pseudo-continuum-normalized APOGEE spectrum, and orange denotes the renormalized spectrum we use in our library. The gaps at 15810 Å and 16440 Å correspond to gaps between APOGEE's detectors.

combined GC spectra are thus in the observed frame, not the stellar rest frame.

3. Generating Simple Stellar Population Models

In this section, we describe the steps in making an SSP spectral model along with how we use each ingredient. We adopt the isochrone synthesis method based on Equation (1) from Section 2 of Conroy (2013):

$$f_{\text{SSP}}(t, Z) = \int_{m_{up}(t)}^{m_{to}} f_{\text{star}}[T_{\text{eff}}(M), \log g(M)|t, Z] \phi(M) dM,$$
(2)

where f_{star} is the spectrum of a star with an initial stellar mass M. The isochrones with an IMF $\phi(M)$ relate the T_{eff} — $\log g$ distributions to an age (t) and chemical composition (Z). The model spectrum f_{SSP} represents the integration (from a lower limit m_{lo} , usually considered to be the hydrogen-burning limit, to an upper limit $m_{\text{up}}(t)$ imposed by stellar evolution) of all the individual spectra from APOGEE along the isochrone, weighted by the fractional luminosity at a given T_{eff} and $\log g$ from the isochrone in the H-R diagram.

The isochrones for our SSP generation span a range in age, [M/H], and $[\alpha/M]$ as described in Section 4.

3.1. Generating Synthetic Stellar Populations

Using an isochrone at a given [M/H] and $[\alpha/M]$, we generate an SSP using the Kroupa (2001) IMF with an initial mass of $10^6 M_{\odot}$. Based on tests we ran using different initial masses (e.g., Beerman et al. 2012) from $10^5 M_{\odot}$ – $10^8 M_{\odot}$, $10^6 M_{\odot}$ was selected as the minimum one needed to ensure that multiple SSPs generated from the same isochrone did not differ in the total number of stars or total luminosity by more than 1%, due to stochastic sampling.

Our synthetic SSPs are generated using a package called PyPopStar (Hosek et al. 2020). This is a Python package that generates a synthetic single-age, single-metallicity population. We generate the synthetic SSP using our isochrones (age, metallicity, and mass) and the initial mass of $10^6\,M_\odot$. The conditions to generate the SSP are:

- 1. Isochrone object: isochrones from Padova or MIST (Section 2.1).
- 2. Initial mass = $10^6 M_{\odot}$
- 3. IMF = Kroupa (2001)
- 4. Stellar multiplicity: defines the properties of multiple systems in a population based on the IMF. This function defines how the stellar masses influence the synthetic population. We use "MultiplicityUnresolved()" with parameters defined in Lu et al. (2013).
- 5. Synthetic star clusters: using the isochrone object, IMF, and the initial mass, we use the resolved star cluster function "ResolvedCluster()," which interpolates the isochrone points within the mass limits to generate the synthetic population.

Each synthetic SSP generated is characterized by an age, [M/H], and [α /M] and describes the $T_{\rm eff}$, log g, and luminosity of stars at a given mass of $10^6 \, M_{\odot}$.

3.2. Parameter Grid for SSP Spectral Model Generation

To construct our SSP spectral models (referred to as A-LIST models from here on), we need to obtain spectra that represent the simulated stars in a 4D parameter space ($T_{\rm eff}$, $\log g$, [M/H], and [α /M]) for each age, [M/H], and [α /M] isochrone. For this, we define 4D bins that span the range of $T_{\rm eff}$, $\log g$, [M/H], and [α /M] needed for the simulated stars. We define bin sizes such that the stars in each bin have on average <1% difference between their normalized spectra and the bin's median spectrum:

- 1. Effective temperature ($T_{\rm eff}$): the full width of the bin $\Delta T_{\rm eff} = 50~{\rm K}$ for $3000~{\rm K} \leqslant T_{\rm eff} \leqslant 5000~{\rm K}$ and the full width of the bin $\Delta T_{\rm eff} = 150~{\rm K}$ for $5000~{\rm K} \leqslant T_{\rm eff} \leqslant 10,000~{\rm K}$. We use a larger bin size for the hotter stars to increase the number of stars per bin (and the number of occupied bins), after confirming that the spectral variations within the bin are still within 1%.
- 2. Surface gravity $(\log g)$: $\Delta \log g = 0.2$ dex for $-1 < \log g < 5$.
- 3. Metallicity ([M/H]): Δ [M/H] = 0.3 dex for $-2.3 \le [M/H] < -1.1$ and Δ [M/H] = 0.2 dex for $-1.1 \le [M/H] \le +0.5$.

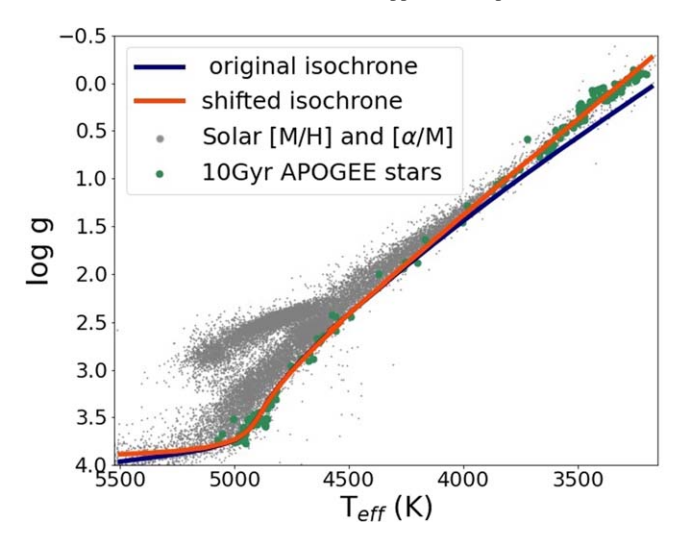


Figure 4. Example of shifting an isochrone to account for the $\log g$ offset (Section 3.3). The isochrone used here has an age of 10 Gyr, solar [M/H], and solar $\lceil \alpha/M \rceil$. The original isochrone is shown in blue. The isochrone is shifted by a function defined by the offset between the stars (solar [M/H], solar $\lceil \alpha/M \rceil$ shown in gray) of the appropriate age (big green points) and the isochrone points. The shifted isochrone is shown in orange.

4. α abundance ($\lceil \alpha/M \rceil$): we define our $\lceil \alpha/M \rceil$ bins based on the $T_{\rm eff}$ of the stars. For all stars having $T_{\rm eff} \leqslant 5700~{\rm K}$ and $-0.25 \leqslant \lceil \alpha/M \rceil < +0.45$, $\Delta \lceil \alpha/M \rceil = 0.1$ dex. For hotter temperatures $T_{\rm eff} > 5700~{\rm K}$ (i.e., the mainsequence stars), there are insufficient α -enhanced stars in our sample. However, because these hot stars have weaker lines, we found that the spectral variations at a given $\lceil M/H \rceil$, $\log g$, and $T_{\rm eff}$ bin across all $\lceil \alpha/M \rceil$ are still within 1% at these temperatures. Therefore, for these hot temperature bins, we select all stars regardless of α enhancement in a given $\lceil M/H \rceil$, $T_{\rm eff}$ and $\log g$ bin.

3.3. Surface Gravity Offset

When matching both the Padova and MIST isochrones with the empirical stellar library, we find that there are offsets in surface gravity and temperature along the upper part of the red giant branch (RGB). Similar offsets along the upper RGB have been seen in previous work (e.g., Serenelli et al. 2017; Durbin et al. 2020). The uncertainties in the APOGEE log g are too small to account for these offsets, and the size of the offset varies for the different isochrone sets. Hence, to account for this difference, we shift the isochrone by a function defined by the offset between the stars and the isochrone in the RGB phase of evolution.

For each isochrone corresponding to an age, [M/H], and $[\alpha/M]$, we select the APOGEE stars having the same [M/H] and $[\alpha/M]$. Based on the astroNN ages for APOGEE (Section 2.3), we further select stars that are the closest 10% in age to the isochrone. We then calculate the $\log g$ offset in the RGB evolutionary phase of the isochrone (3000 $K \leqslant T_{\rm eff} \leqslant 5500\,K$) from the mean $\log g$ of the APOGEE stars in each temperature bin (Section 3.2). A third-order polynomial is fit to this offset, and the isochrones are shifted to match the APOGEE stars.

Figure 4 shows an example of this process. A 10 Gyr, solar [M/H], solar $[\alpha/M]$ isochrone (blue line) is plotted over the solar [M/H], solar $[\alpha/M]$ APOGEE stars (\sim 39,000 stars;

shown as small gray points). The 10% of APOGEE stars with astroNN ages closest to 10 Gyr in the RGB evolutionary phase are shown as big green points (\sim 170 stars). The isochrone shifted in log g to match these points is shown as an orange line. For the shift shown in Figure 4, the standard deviation of the difference between the shifted and unshifted spectra is just 0.14%, while the maximum difference in the spectra is \sim 1%.

3.4. Incorporating the APOGEE Spectral Library

To obtain the integrated light model spectrum of an SSP, the synthetic SSPs generated from the isochrones and the APOGEE stars are both binned in the 4D cube (Section 3.2). Each bin is assigned a weight based on the fractional luminosity it contains, from the total synthetic SSP. In addition, each bin is assigned a median spectrum calculated from all of the APOGEE stars in that bin. Then, the final A-LIST model SSP is obtained by summing the median spectra from all the bins, each scaled by its luminosity weight determined from the binned synthetic SSP.

4. Description of A-LIST Models

In this section, we describe the integrated NIR SSP model spectra created from APOGEE and synthetic SSPs. A-LIST contains SSP spectral models based on Padova isochrones and MIST isochrones, available at a range of ages, metallicities, and α abundances:

- 1. Age (Gyr): 2.0, 3.0, 4.0, 5.0, 6.0, 7.0, 8.0, 9.0, 10.0, 11.0, 12.0
- 2. Metallicity ([M/H]): -2.2, -1.9, -1.6, -1.3, -1.0, -0.8, -0.6, -0.4, -0.2, 0.0, +0.2, +0.4
- 3. α abundances ([α /M]): -0.2, -0.1, 0.0, +0.1, +0.2, +0.3, +0.4

Figure 5 shows examples of 10 Gyr old, Padova-based A-LIST spectral models varying in [M/H] and [α/M] across the full range of [M/H]. The abundance change in the models is reflected in many of the absorption lines, strengthening from metal poor to metal rich, e.g., in the Fe lines visible at \sim 15900 Å. Figure 6(a) shows examples of 10 Gyr old, Padova-based A-LIST spectral models with [M/H] = - 0.4 and different [α/M]. An example of how models change with [α/M] can be seen at the CO band heads at 15990 and 16180 Å, as well as in the Mg line at 16365 Å. In all cases, these α -element lines increase in strength from α -poor to α -rich models.

Figure 6(b) shows the mean equivalent width (EW) of lines of different elements for each of the high fractional luminosity A-LIST models (>0.5; see Section 4.1.1) shown in Figure 6(a). We calculate the EW of nonblended absorption lines in the model spectra corresponding to Fe, Al, and Mn (non- α elements) and to Mg and Si (α elements). Each of the points shown in Figure 6(b) is the mean value of all the individual elemental EWs normalized to their element's $[\alpha/M] = 0$ values. The total number of lines represented in this plot are 74 for Fe, 8 for Mn, 5 for Al, 13 for Mg, and 18 for Si. We see an increase in the α -element EWs (solid lines), in contrast to the non- α -element EWs (dashed lines). Indeed, the non- α EWs decrease at higher $[\alpha/M]$, as expected with scaled-solar [M/H] held constant.

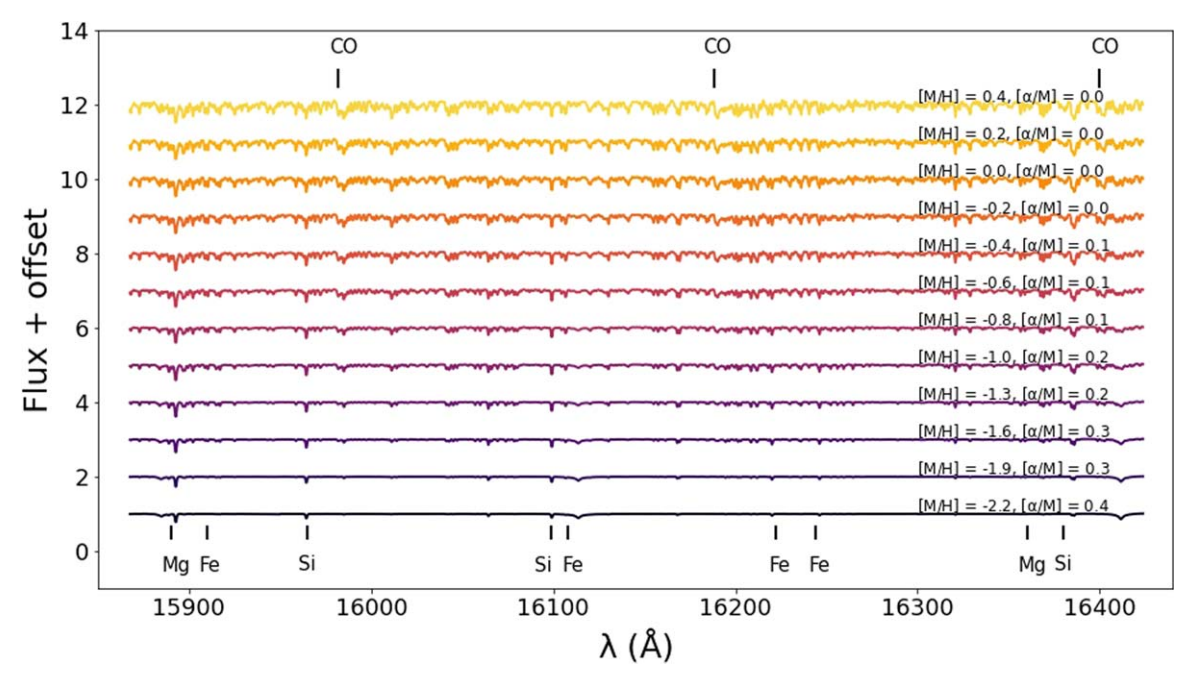


Figure 5. Model spectra generated for 10 Gyr, Padova-based SSPs ranging in [M/H] and $[\alpha/M]$. Shown here is a small wavelength range (15850–16440 Å). For each [M/H], the model with the highest recovered fractional luminosity (Section 4.1.1, Figure 8(a)) is shown. Some Mg, Si, and Fe lines are highlighted for this wavelength range along with the CO band heads.

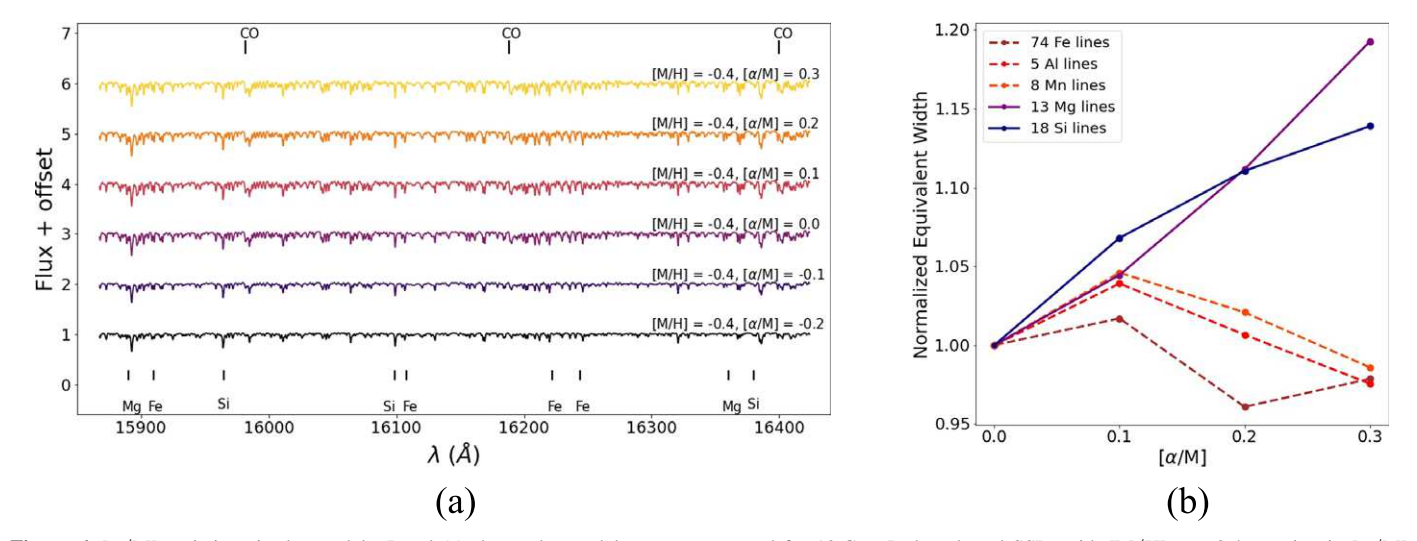


Figure 6. $[\alpha/M]$ variations in the models. Panel (a) shows the model spectra generated for 10 Gyr, Padova-based SSPs with [M/H] = -0.4, varying in $[\alpha/M]$. Shown here is a small wavelength range (15850–16440 Å) with some of the major α -bearing molecular bands and atomic lines labeled. We see that the absorption lines get deeper from α -poor to α -rich models. Some of the Mg, Si, and Fe lines used in panel (b) are highlighted, along with the CO band heads. Panel (b) shows the variations in line equivalent widths (solid: α lines and dashed: non- α lines) for solar- α and α -enhanced models. The circles are the means of all the EWs of the respective element, normalized by the mean EW of the same element at solar α .

For each model, we also provide a spectrum that characterizes the standard deviation of the individual stellar spectra in each 4D bin used to create that model. The standard deviation of the spectra is measured at each spectral pixel in each 4D bin, and then these individual bin standard deviation spectra are added together using the same weights as the model spectra. This "variance" spectrum has a typical value of 1% across all ages, [M/H], and [α /M]. However, as we show in the next section, the dominant uncertainties in our model spectra are due to a lack of APOGEE stellar spectra for some

models in $\log g$ - $T_{\rm eff}$ bins, which are not reflected in the provided variance spectrum.

4.1. Metrics for Assessing the Accuracy of A-LIST Models

One simple method to validate the A-LIST models is to compare the differences between the models and an ideal synthetic stellar population model. In this section, we assume the synthetic SSPs to fully represent a stellar population of a given age, [M/H], and [α /M]. The differences observed are due to either a lack of available stars in our empirical

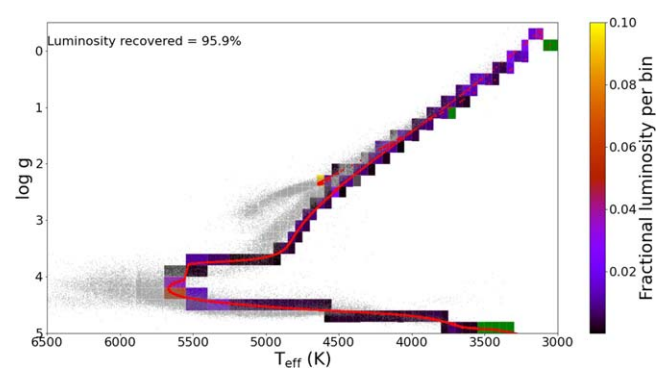


Figure 7. H-R diagram of a 10 Gyr, solar-[M/H], solar- $[\alpha/M]$ SSP, colored by the fraction of the total synthetic population luminosity in each bin. The APOGEE stars for this [M/H] and $[\alpha/M]$ bin are shown as gray points. The SSP based on a Padova isochrone (for the given age, [M/H] and $[\alpha/M]$) is shown as red points.

stellar library or our binning methods. We discuss the similarities between A-LIST models and the synthetic SSPs in terms of the luminosity recovered (Section 4.1.1) and the average $T_{\rm eff}$ (Section 4.1.2). We also discuss the variation of the average metallicity and α abundance of A-LIST models from the defined bin center (Section 4.1.3).

4.1.1. Fraction of the Synthetic SSP Luminosity Represented in A-LIST Models

One important aspect of the A-LIST spectral models is how much of the total synthetic SSP luminosity is represented. Figure 7 shows an H-R diagram that describes how we compute the fractional luminosity from the synthetic SSP for one A-LIST model (10 Gyr, solar [M/H], solar [α /M]). The APOGEE stars with the same [M/H] and [α /M] are shown as black points. The synthetic SSP is shown as red points. From this synthetic SSP, we calculate the fraction of light in each of our spectral bins (Section 3.2), which is indicated by the color of the bin. Bins that have a nonzero fraction of luminosity but no APOGEE stars in them—i.e., bins that are not represented in the final A-LIST model spectrum—are colored green. There are \approx 8000 stars at solar [M/H] and solar [α /M] (Figure 2(b)), enabling the high fractional luminosity here (\sim 0.97).

Figure 8(a) shows the fractional luminosity of each 10 Gyr A-LIST spectral model as a function of [M/H] and $[\alpha/M]$. In general, the highest fractional luminosities coincide with the most-populated parts of chemical abundance space in the APOGEE sample. In Section 5.4, we discuss in detail how the fractional luminosity captured by the A-LIST models impacts the model properties and fits. We demonstrate there that the models with luminosity fraction below 0.32 are less reliable, and thus in Figure 8(a), we highlight the reliable models with a white dashed outline.

4.1.2. Average Temperature of A-LIST Models

Figure 8(b) shows the difference in the luminosity-weighted average $T_{\rm eff}$ for 10 Gyr A-LIST models, as a function of [M/H] and $[\alpha/{\rm M}]$, between the Padova-based synthetic SSPs and corresponding A-LIST models. The large negative differences are due to a lack of cool (\sim 3500 K), low-surface-gravity stars in our APOGEE sample at particular metallicity and α combinations (e.g., at [M/H] = 0.0 and $[\alpha/{\rm M}]$ = - 0.1, where

 $\Delta T_{\rm eff} \sim -400$ K). The large positive differences are due to a lack of hot (\sim 7000 K) main-sequence stars; these are mostly in our lower-metallicity models (e.g., at [M/H] = -1.3 and [α /M] = 0.1, where $\Delta T_{\rm eff} \sim 300$ K). In Section 5.4, we assess how the change in luminosity-weighted average $T_{\rm eff}$ impacts the model properties.

In Section 3.2, we define the [M/H] and $[\alpha/M]$ bins in our hypercube based on the desired model grid values. These bin values are assigned to the generated spectral models, assuming that the mean [M/H] and $[\alpha/M]$ values of stars in the bin are the same as those of the bin center (e.g., in the [M/H] bin with bin edges $-1.1 \le [\mathrm{M/H}] < -0.9$, we assume the mean $[\mathrm{M/H}] = -1.0$).

However, due to the nonuniform distribution of APOGEE stars across our bins, our mean [M/H] and $[\alpha/M]$ are sometimes offset from the bin centers as shown in Figure 8(c). The red points indicate the mean [M/H] and $[\alpha/M]$ values for 10 Gyr Padova-based A-LIST models. These values are obtained by calculating the average [M/H] and $[\alpha/M]$ weighted by the fractional luminosity of all the APOGEE stars with $T_{\rm eff} \lesssim 5700$ K (i.e., all stars that are binned by $[\alpha/M]$). The bin centers are shown by the inner red lines. For example, in the $[\alpha/M] = -0.1$ and [M/H] = -1.0bin, we select stars with $-1.1 \le [M/H] < -0.9$. Although the mean [M/H] = -1.0 based on the bin edges, the actual mean [M/H] = -1.07, based on the stars available in the bin. The average absolute offset from the input [M/H] is 0.013 for all models with luminosity fraction above 0.32 (including those inside the dashed line in Figure 8(c)), while for $[\alpha/M]$ this average absolute offset is 0.018.

4.2. Difference between Padova and MIST Based Models

A-LIST consists of spectral models generated using two different isochrone sets: Padova and MIST (Section 2.1). Figure 9 shows a comparison between 10 Gyr, solar [M/H], solar [α /M] MIST-based (shown in blue) and Padova-based (shown in fuchsia) A-LIST model spectra. The maximum difference is \sim 3%, and the standard deviation of the difference is <1%.

The difference between Padova-based and MIST-based model spectra arises from the differences in the isochrones, primarily from the cooler-temperature bins (briefly explained in Section 2.1). For example, in Figure 9, the TP-AGB stars in the MIST-based population have $T_{\rm eff} \sim 3200$ K, and in the Padovabased one, they have $T_{\rm eff} \sim 3100$ K. This ~ 100 K difference leads to deeper absorption lines in the Padova models, with a maximum difference of 3%. In Section 5.2, we show that while overall both models recover the metallicities and α abundances of globular clusters, these model differences lead to small differences in measurements for individual clusters. We note that, consistent with the TP-AGB star difference discussed above, the Padova models typically have luminosity-weighted effective temperatures that are ~ 100 K hotter than the MIST models with the same population parameters.

Figure 10 shows the standard deviation in the difference between the 10 Gyr MIST-based and Padova-based A-LIST models models as a function of [M/H] and $[\alpha/M]$. We see that the difference in the models for the most-populated parts of the chemical abundance space is <1.5% of the normalized flux.

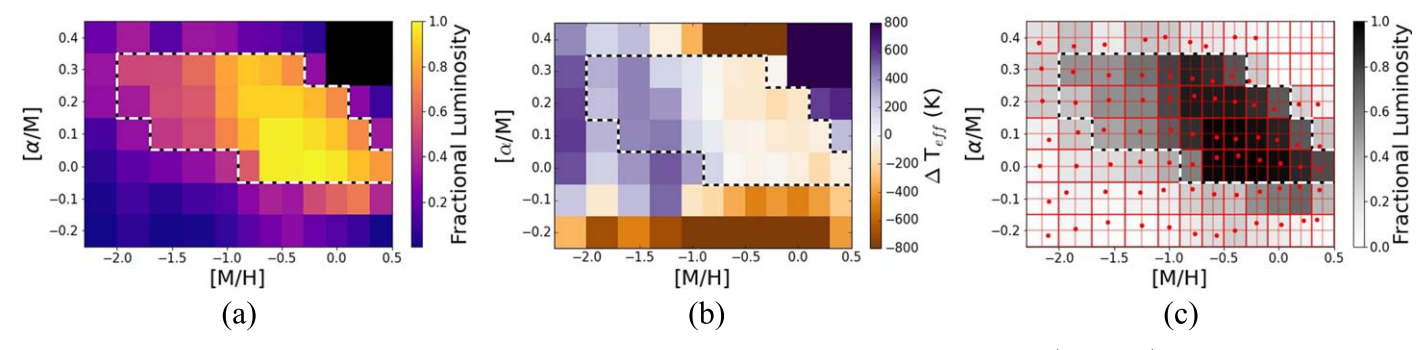


Figure 8. Reliability of 10 Gyr, Padova-based A-LIST models using the Padova-based synthetic SSPs as a function of [M/H] and $[\alpha/M]$. The bins that lie within the black and white dashed lines in each panel are the models that we recommend using (Section 5.4). Panel (a) shows the fractional luminosity of the A-LIST models generated using 10 Gyr synthetic SSPs (Section 4.1.1). Panel (b) shows the difference in the luminosity-weighted average temperature between 10 Gyr Padova-based synthetic SSPs and their corresponding A-LIST models (Section 4.1.2). Panel (c) shows the fractional luminosity of each A-LIST model (as in panel (a)) with the mean metallicity and α -abundance values of each A-LIST model (Section 4.1.3). The red dots indicate the luminosity-weighted average values in each bin, and the red lines indicate the bin centers. These values are calculated excluding stars with $T_{\rm eff} > 5700$ K (Section 3.2).

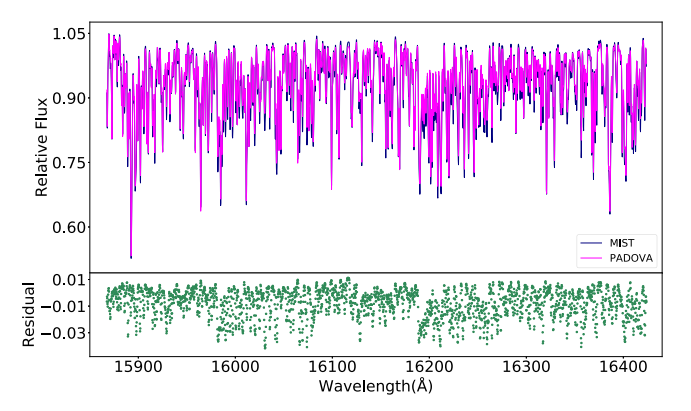


Figure 9. Difference between a 10 Gyr, solar [M/H], solar [α /M] Padovabased model (fuchsia) and MIST-based model (dark blue). Shown here are the model spectra for a small wavelength range (15850–16440 Å). The residual (in green) is a simple difference between the two models.

The bins with larger deviations (>1.5%) correspond to the least-populated parts of chemical abundance space of the APOGEE stars (like very metal-poor, solar- α bins and metalrich, α -rich bins), which also correspond to regions lying outside the white "high-reliability" contour (Section 5.4).

5. Spectral Model Validation

In this section, we validate A-LIST models by recovering the kinematics, [M/H], and $[\alpha/M]$ of M31 GCs and by comparing our A-LIST spectral library to the lower-resolution E-MILES (Vazdekis et al. 2016) library.

5.1. Fitting procedure

We use the pPXF (Cappellari et al. 2009; Cappellari 2017), a full-spectrum fitting code that calculates stellar kinematics and stellar population parameters from absorption-line spectra using a maximum penalized likelihood approach. We compute velocities, dispersions, and stellar population parameters for the GCs using A-LIST as templates, and to compare the age and [M/H] of our high-resolution models with a low-resolution spectral library.

5.2. M31 GCs

GCs are not perfect SSPs (e.g., Gratton et al. 2012), but are very close to being so; hence, they are useful for validating our A-LIST models by recovering the properties of previously

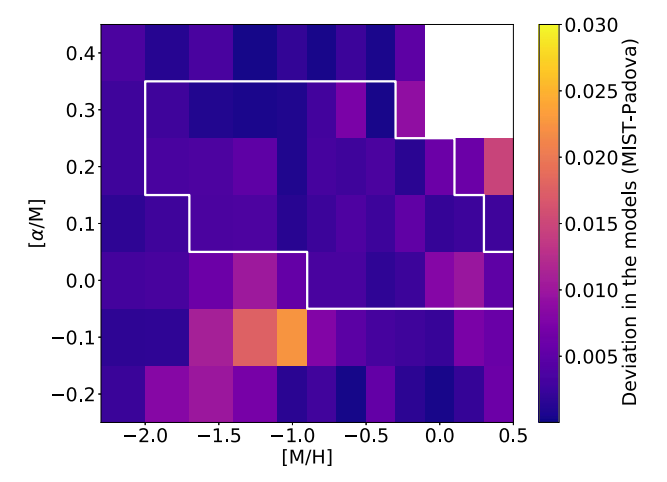


Figure 10. The standard deviation of the difference between the 10 Gyr Padova- and MIST-based spectral models for each bin in [M/H] and $[\alpha/M]$. The white line is the same as the white dashed line shown in Figure 8(a). A small difference is observed for the models of each age, [M/H], and $[\alpha/M]$.

studied clusters observed by APOGEE (Section 2.3). We select 32 GCs with $10 \le S/N \le 150$ (7 of which were studied in Sakari et al. 2016).

To determine the properties of the GCs, we fit each of our A-LIST models one at a time to the GCs over the wavelength range of the green and red detectors (i.e., 15850–16960 Å). We do not use the blue detector due to the presence of high persistence in many spectra (see Section 3.4 of Majewski et al. 2017). We take the likelihood-weighted average for age, [M/H], and $[\alpha/M]$ from the three fits with smallest reduced- χ^2 values. We use all A-LIST models with age >6 Gyr to reduce the time needed to run the code. The uncertainties on these fits are calculated in two different ways: for radial velocity and the velocity dispersion, the systematic uncertainty on the best-fit model is determined by a simple bootstrapping for n = 100. For [M/H] and $[\alpha/M]$, we calculate the uncertainty using the relative χ^2 of the best-fit model relative to other models. More specifically, we derive our uncertainties in [M/H] and $[\alpha/M]$ by using a $\Delta \chi^2$ limit corresponding to a 1σ uncertainty, deriving both lower and upper limits.

Table 1 shows the radial velocity, velocity dispersion, [M/H], $[\alpha/M]$, and age of the M31 GCs determined using the A-LIST library, both Padova-based and MIST-based, along with the uncertainties.

Table 1
Table Containing the Age, [M/H], [α /M], RV, and σ Retrieved from Fitting the Padova-based and MIST-based A-LIST Spectral Models to 32 Selected M31 GCs

| Globular cluster | S/N | MIST-based SSP | | | | | Padova-based SSP | | | | |
|------------------|-----|-----------------------------|--|-------------------------------|---------------------|----------------------|-----------------------------|-------------------------------------|----------------------|---------------------|-----------------------|
| | | RV (km s ⁻¹) | $\frac{\sigma}{(\mathrm{km\ s}^{-1})}$ | [M/H] | $[\alpha/M]$ | Age (Gyr) | RV (km s ⁻¹) | $\frac{\sigma}{(\text{km s}^{-1})}$ | [M/H] | $[\alpha/M]$ | Age (Gyr) |
| B006-G058 | 25 | -235.9 ± 0.3 | 12.9 ± 0.4 | $-0.5^{+0.3}_{-0.4}$ | $0.2^{+0.2}_{-0.1}$ | $10.3^{+1.7}_{-2.1}$ | -235.9 ± 0.3 | 13.0 ± 0.2 | $-0.6^{+0.3}_{-0.3}$ | $0.3^{+0.1}_{-0.1}$ | $10.3^{+1.1}_{-1.6}$ |
| B012-G064 | 23 | -362.1 ± 1.9 | 13.7 ± 2.3 | $-1.6^{+0.8}_{-0.1}$ | $0.1^{+0.3}_{+0.3}$ | $10.3^{+1.2}_{-1.5}$ | -361.6 ± 1.9 | 17.4 ± 2.7 | $-1.8^{+0.5}_{-0.2}$ | $0.1^{+0.2}_{+0.1}$ | $10.3^{+2.1}_{-1.2}$ |
| B023-G078 | 180 | -440.3 ± 0.4 | 28.5 ± 0.4 | $-0.5^{+0.3}_{-0.1}$ | $0.1^{+0.2}_{+0.1}$ | $6.7^{+2.6}_{-2.3}$ | -442.3 ± 0.6 | 29.5 ± 0.4 | $-0.5^{+0.3}_{-0.1}$ | $0.1^{+0.1}_{-0.1}$ | $6.3^{+3.5}_{-3.1}$ |
| B025-G084 | 10 | -202.7 ± 2.6 | 11.8 ± 2.9 | $-1.5^{+0.5}_{-0.1}$ | $0.1^{+0.1}_{-0.1}$ | $8.3^{+0.7}_{-2.2}$ | -202.2 ± 0.8 | 8.8 ± 0.2 | $-0.9^{+0.5}_{-0.3}$ | $0.2^{+0.1}_{-0.1}$ | $8.4^{+1.3}_{-1.2}$ |
| B045-G108 | 17 | -426.1 ± 0.5 | 11.4 ± 0.5 | $-0.9^{+0.2}_{-0.1}$ | $0.2^{+0.1}_{-0.1}$ | $10.6^{+2.4}_{-2.5}$ | -426.3 ± 0.3 | 10.9 ± 0.3 | $-1.0^{+0.3}_{-0.3}$ | $0.2^{+0.2}_{-0.2}$ | $10.6^{+2.3}_{-2.5}$ |
| B063-G124 | 34 | -304.1 ± 0.4 | 18.2 ± 0.5 | $-1.0^{+0.1}_{-0.5}$ | $0.2^{+0.1}_{-0.1}$ | $10.3^{+1.4}_{-2.6}$ | -304.1 ± 0.3 | 18.6 ± 0.3 | $-1.0^{+0.3}_{-0.3}$ | $0.2^{+0.2}_{-0.2}$ | $8.3^{+1.2}_{-1.5}$ |
| B068-G130 | 23 | -321.6 ± 0.3 | 9.1 ± 0.3 | $-0.2^{+0.3}_{-0.3}$ | $0.2^{+0.1}_{-0.1}$ | $9.7^{+1.2}_{-1.8}$ | -321.6 ± 0.3 | 9.5 ± 0.3 | $-0.2^{+0.1}_{-0.3}$ | $0.2^{+0.1}_{-0.1}$ | $9.7^{+2.6}_{-2.7}$ |
| B088-G150 | 32 | -482.4 ± 1.5 | 9.8 ± 1.5 | $-1.6^{+0.7}_{-0.1}$ | $0.0^{+0.1}_{-0.1}$ | $8.5^{+2.6}_{-0.8}$ | $-484.7.0 \pm 1.4$ | 16.2 ± 1.3 | $-1.6^{+0.1}_{-0.3}$ | $0.1^{+0.2}_{-0.1}$ | $8.8^{+2.3}_{-1.2}$ |
| B103-G165 | 98 | -367.6 ± 0.3 | 17.3 ± 0.3 | $-0.4^{+0.3}_{-0.4}$ | $0.3^{+0.1}_{-0.1}$ | $11.3^{+0.9}_{-1.2}$ | -367.3 ± 0.2 | 17.3 ± 0.2 | $-0.6^{+0.4}_{-0.2}$ | $0.2^{+0.2}_{-0.2}$ | $10.7^{+0.5}_{-2.6}$ |
| B107-G169 | 47 | -332.8 ± 0.8 | 16.3 ± 1.1 | $-1.0^{+0.2}_{-0.2}$ | $0.1^{+0.1}_{-0.1}$ | $11.3^{+0.3}_{-2.1}$ | -333.2 ± 0.8 | 15.9 ± 1.1 | $-1.2^{+0.1}_{-0.1}$ | $0.2^{+0.2}_{-0.1}$ | $11.3^{+1.2}_{-1.3}$ |
| B109-G170 | 23 | -620.3 ± 0.2 | 7.7 ± 0.3 | $-0.3^{+0.5}_{-0.1}$ | $0.3^{+0.1}_{-0.1}$ | $10.1^{+2.1}_{-1.2}$ | -620.3 ± 0.2 | 7.5 ± 0.3 | $-0.3^{+0.3}_{-0.3}$ | $0.3^{+0.1}_{-0.1}$ | $10.0^{+0.8}_{-2.3}$ |
| B112-G174 | 20 | -276.5 ± 0.2 | 10.2 ± 0.3 | $-0.5^{+0.3}_{-0.1}$ | $0.2^{+0.2}_{-0.2}$ | $9.0^{+2.4}_{-3.4}$ | -276.7 ± 0.2 | 11.5 ± 0.3 | $-0.2^{+0.2}_{-0.2}$ | $0.1^{+0.2}_{-0.1}$ | $10.3^{+3.8}_{-0.8}$ |
| B115-G177 | 36 | -599.7 ± 0.3 | 13.1 ± 0.3 | $-0.3^{+0.3}_{-0.2}$ | $0.2^{+0.1}_{-0.1}$ | $10.8^{+1.7}_{-3.2}$ | -599.7 ± 0.2 | 13.1 ± 0.2 | $-0.2^{+0.3}_{-0.3}$ | $0.2^{+0.1}_{-0.1}$ | $10.6^{+2.3}_{-0.7}$ |
| B127-G185 | 151 | -527.8 ± 0.4 | 23.4 ± 0.4 | $-0.6^{+0.1}_{-0.1}$ | $0.2^{+0.1}_{-0.1}$ | $10.1^{+0.6}_{-0.8}$ | -527.8 ± 0.2 | 23.2 ± 0.3 | $-0.7^{+0.2}_{-0.2}$ | $0.2^{+0.1}_{-0.1}$ | $10.3^{+0.8}_{-2.3}$ |
| B128-G187 | 15 | -382.4 ± 0.8 | 11.5 ± 0.9 | $-0.6^{+0.1}_{-0.3}$ | $0.3^{+0.1}_{-0.1}$ | $10.9^{+0.3}_{-0.2}$ | -382.3 ± 0.8 | 11.7 ± 0.9 | $-0.6^{+0.4}_{-0.3}$ | $0.2^{+0.1}_{-0.1}$ | $11.1^{+0.9}_{-0.8}$ |
| B129 | 59 | -413.7 ± 0.5 | 18.2 ± 0.6 | $-1.0^{+0.2}_{-0.4}$ | $0.2^{+0.1}_{-0.2}$ | $10.4^{+2.5}_{-2.3}$ | -43.7 ± 0.3 | 18.2 ± 0.3 | $-0.8^{+0.1}_{-0.1}$ | $0.2^{+0.1}_{-0.2}$ | $9.6^{+3.7}_{-3.7}$ |
| B131-G189 | 105 | -466.4 ± 0.6 | 22.7 ± 0.6 | $-0.5^{+0.1}_{-0.1}$ | $0.2^{+0.1}_{-0.1}$ | $9.3^{+2.6}_{-1.8}$ | -466.3 ± 0.4 | 22.8 ± 0.6 | $-0.7^{+0.3}_{-0.2}$ | $0.2^{+0.1}_{-0.2}$ | $9.1^{+0.8}_{-2.3}$ |
| B151-G205 | 125 | -324.5 ± 0.5 | 22.1 ± 0.4 | $-0.6^{+0.2}_{-0.2}$ | $0.1^{+0.1}_{-0.1}$ | $9.6^{+2.7}_{-2.1}$ | -342.3 ± 0.3 | 22.3 ± 0.2 | $-0.7^{+0.1}_{-0.3}$ | $0.2^{+0.1}_{-0.1}$ | $10.3^{+1.0}_{-12}$ |
| B153 | 50 | -246.9 ± 0.3 | 11.9 ± 0.4 | $-0.3^{+0.2}_{-0.2}$ | $0.2^{+0.1}_{-0.1}$ | $10.3^{+2.5}_{-2.6}$ | -246.9 ± 0.2 | 11.9 ± 0.2 | $-0.3^{+0.2}_{-0.3}$ | $0.3^{+0.1}_{-0.1}$ | $10.8^{+2.1}_{-2.7}$ |
| B171-G222 | 72 | -269.1 ± 0.3 | 14.6 ± 0.3 | $-0.4^{+0.1}_{-0.2}$ | $0.2^{+0.1}_{-0.1}$ | $10.1^{+0.4}_{-0.6}$ | -269.1 ± 0.2 | 14.5 ± 0.2 | $-0.4^{+0.2}_{-0.3}$ | $0.2^{+0.1}_{-0.1}$ | $9.8^{+1.8}_{-0.5}$ |
| B180-G231 | 12 | -198.9 ± 0.3 | 9.1 ± 0.9 | $-1.0^{+0.4}_{-0.4}$ | $0.2^{+0.1}_{-0.1}$ | $9.0^{+3.2}_{-2.4}$ | -198.9 ± 0.7 | 9.2 ± 0.9 | $-1.0^{+0.5}_{-0.5}$ | $0.1^{+0.1}_{-0.2}$ | $9.0^{+1.2}_{-1.2}$ |
| B190-G241 | 10 | -88.8 ± 0.3 | 6.8 ± 1.7 | $-1.3^{+0.3}_{-0.5}$ | $0.2^{+0.2}_{-0.1}$ | $10.6^{+1.0}_{-2.1}$ | -88.3 ± 0.4 | 7.1 ± 1.8 | $-1.1^{+0.7}_{-0.3}$ | $0.1^{+0.2}_{-0.1}$ | $10.4^{+0.3}_{-1.4}$ |
| B193-G244 | 29 | -62.1 ± 0.3 | 17.2 ± 0.3 | $-0.2^{+0.3}_{-0.1}$ | $0.2^{+0.2}_{-0.2}$ | $8.8^{+2.4}_{-1.4}$ | -62.1 ± 0.2 | 16.8 ± 0.1 | $-0.2^{+0.2}_{-0.3}$ | $0.3^{+0.2}_{-0.2}$ | $8.6^{+4.6}_{-3.5}$ |
| B206-G257 | 58 | -194.3 ± 0.6 | 16.2 ± 0.7 | $-1.1^{+0.3}_{-0.1}$ | $0.2^{+0.2}_{-0.1}$ | $9.7^{+1.7}_{-1.2}$ | -194.2 ± 0.7 | 16.9 ± 0.1 | $-1.1^{+0.2}_{-0.2}$ | $0.2^{+0.1}_{-0.1}$ | $9.7^{+3.2}_{-1.7}$ |
| B213-G264 | 14 | -572.1 ± 0.9 | 8.7 ± 0.2 | $-0.7^{+0.3}_{-0.2}$ | $0.1^{+0.1}_{-0.1}$ | $9.9^{+0.9}_{-0.8}$ | -572.1 ± 0.3 | 8.9 ± 0.6 | $-0.9^{+0.3}_{-0.3}$ | $0.1^{+0.1}_{-0.1}$ | $10.2^{+1.5}_{-0.6}$ |
| B313-G036 | 19 | -420.3 ± 3.2 | 10.9 ± 3.9 | $-0.8^{+0.3}_{-0.3}$ | $0.1^{+0.1}_{-0.2}$ | $10.0^{+0.7}_{-1.2}$ | -426.2 ± 0.8 | 7.8 ± 1.7 | $-1.2^{+0.6}_{-0.3}$ | $0.1^{+0.2}_{-0.1}$ | $11.00^{+2.7}_{-0.8}$ |
| B373-G305 | 86 | -220.1 ± 0.3 | 12.4 ± 0.3 | $-0.5^{+0.1}_{-0.1}$ | $0.3^{+0.2}_{-0.2}$ | $9.9^{+2.3}_{-2.1}$ | -220.5 ± 0.2 | 13.1 ± 0.8 | $-0.7^{+0.3}_{-0.2}$ | $0.3^{+0.1}_{-0.2}$ | $9.8^{+3.1}_{-0.6}$ |
| B386-G322 | 48 | -393.8 ± 0.5 | 12.8 ± 0.9 | $-1.1^{+0.2}_{-0.1}$ | $0.2^{+0.1}_{-0.2}$ | $9.3^{+3.4}_{-1.3}$ | -393.5 ± 0.9 | 14.3 ± 1.5 | $-1.3^{+0.4}_{-0.1}$ | $0.3^{+0.1}_{-0.2}$ | $9.3^{+3.7}_{-2.6}$ |
| B403-G348 | 40 | -265.6 ± 0.5 | 9.9 ± 0.6 | $-0.9^{+0.1}_{-0.2}$ | $0.1^{+0.2}_{-0.1}$ | $10.4^{+0.4}_{-1.2}$ | -265.5 ± 0.3 | 9.7 ± 0.4 | $-0.9^{+0.3}_{-0.1}$ | $0.0^{+0.2}_{-0.2}$ | $10.2^{+1.2}_{-1.5}$ |
| B407-G352 | 49 | -296.2 ± 0.5 | 9.2 ± 0.4 | $-0.6^{+0.1}_{-0.8}$ | $0.1^{+0.1}_{-0.1}$ | $11.4^{+0.9}_{-0.9}$ | -296.7 ± 0.2 | 9.7 ± 0.9 | $-0.7^{+0.5}_{-0.3}$ | $0.2^{+0.1}_{-0.1}$ | $11.4^{+0.7}_{-1.8}$ |
| B472-D064 | 55 | -115.8 ± 0.5 | 22.8 ± 1.6 | $-1.1\substack{+0.3 \\ -0.1}$ | $0.1^{+0.1}_{-0.1}$ | $9.5^{+1.7}_{-1.6}$ | -116.7 ± 0.3 | 22.5 ± 0.2 | $-1.2^{+0.5}_{-0.2}$ | $0.1^{+0.1}_{-0.1}$ | $9.5^{+2.7}_{-2.2}$ |

Note. The selection of GCs (32 shown here from \sim 185 available) is based on available literature values as well as based on physical pPXF fits with reasonable χ^2 values. We eliminate those GCs that have a very noisy spectra and/or have a continuum issue in their chips.

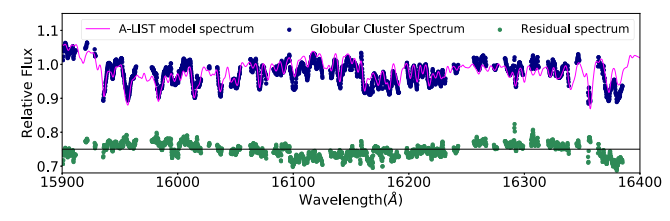


Figure 11. Example of a best-fit model to a high-S/N M31 GC spectrum (B127-G185, S/N = 150). Here we are fitting a 10 Gyr, [M/H] = -0.6, [α /M] = 0.1 A-LIST model spectrum. We note that some regions of the spectra have been excluded from the fit due to the presence of strong sky lines; these sections have been excluded from the fit and are not plotted in the spectrum or residuals.

Figure 11 shows an example of a high-S/N GC spectrum (B127-G185, S/N = 150) with its best-fit A-LIST Padova-based model spectrum, for a small section of the wavelength range (15850–16440 Å). The GC spectrum is first masked for bad sky lines as well as in regions where the error on the flux is high. The residuals are very small (standard deviation $\sim 0.013\%$)

Figure 12 compares our best-fit values from the A-LIST models with literature values. Due to a lack of available $\lceil \alpha/M \rceil$ literature measurements for our M31 GCs, we use $\lceil Mg/Fe \rceil$ derived from the line indices in Schiavon et al. (2012) to compare with A-LIST $\lceil \alpha/M \rceil$. The literature comparison for the other parameters are obtained from Strader et al. (2011) for velocity dispersion and radial velocities and from Caldwell et al. (2011) for $\lceil Fe/H \rceil$. We also include radial velocities, metallicity, and $\lceil \alpha/Fe \rceil$ estimates for these GCs from Sakari et al. (2016).

The dynamical and chemical properties recovered from the A-LIST models agree well with these previous literature values (Table 2). For Padova-based values (MIST-based values in parentheses), we find a median offset (literature—A-LIST) of 0.09 (0.04) in [M/H] and 0.02 (0.02) in [α /M], while the median absolute deviation is 0.1 (0.08) in [M/H] and 0.04 (0.04) in [α /M]. These median absolute deviations are comparable to or smaller than the size of the literature errors on these quantities.

Overall, we find that the MIST-based model metallicities match more closely those of Caldwell et al. (2011), while the Padova-based models give somewhat lower metallicities. This

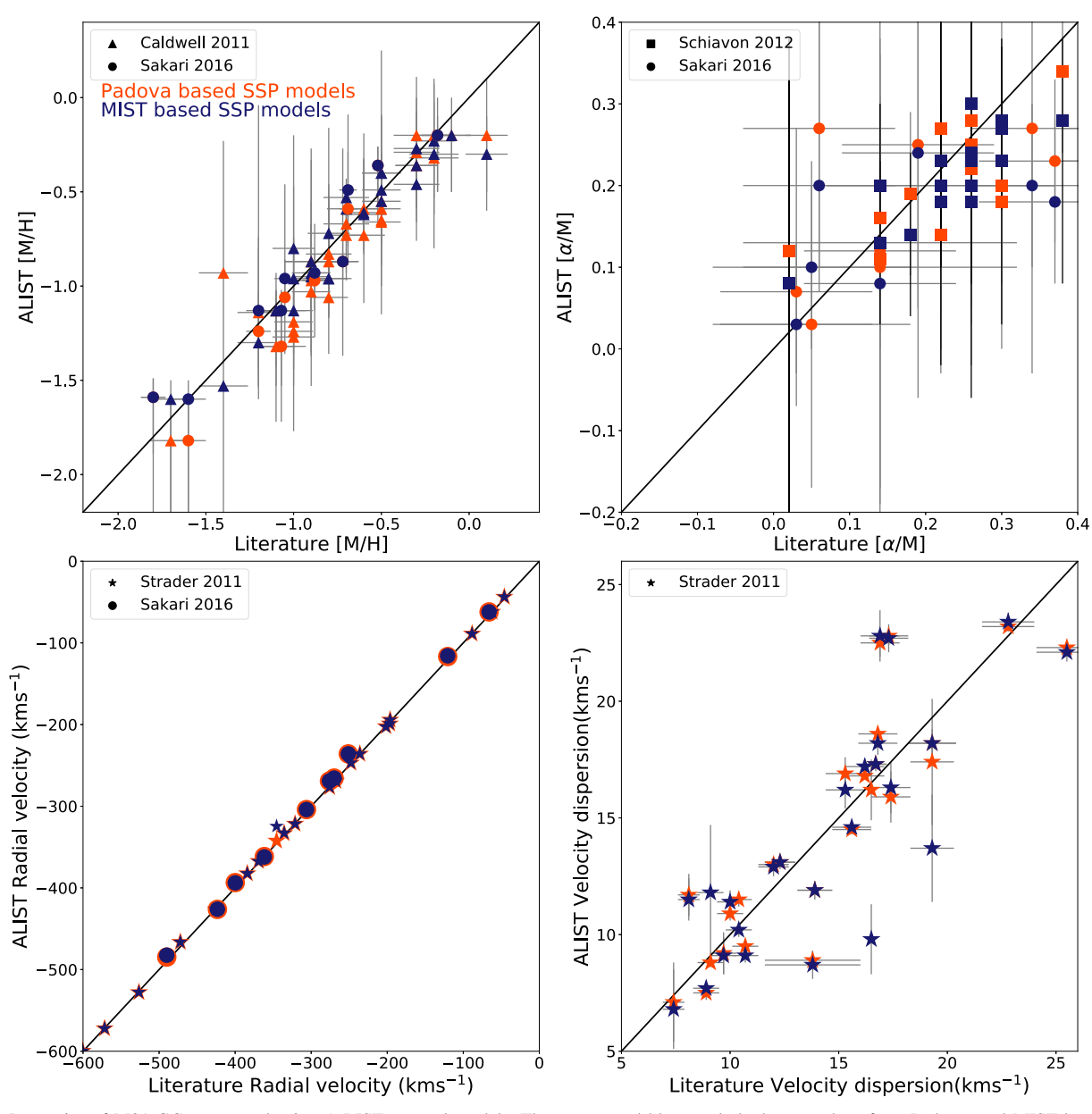


Figure 12. Properties of M31 GCs recovered using A-LIST spectral models. The orange and blue symbols denote values from Padova- and MIST-based A-LIST models, respectively. The symbol shapes indicate the literature source: circles for Sakari et al. (2016), triangles for Caldwell et al. (2011), stars for Strader et al. (2011), and squares for Schiavon et al. (2012).

Table 2
Median Offsets (Literature—A-LIST) and Median Absolute Deviation in A-LIST Parameter Values when Fit to M31 GCs, Compared to Literature Measurements (Figure 12)

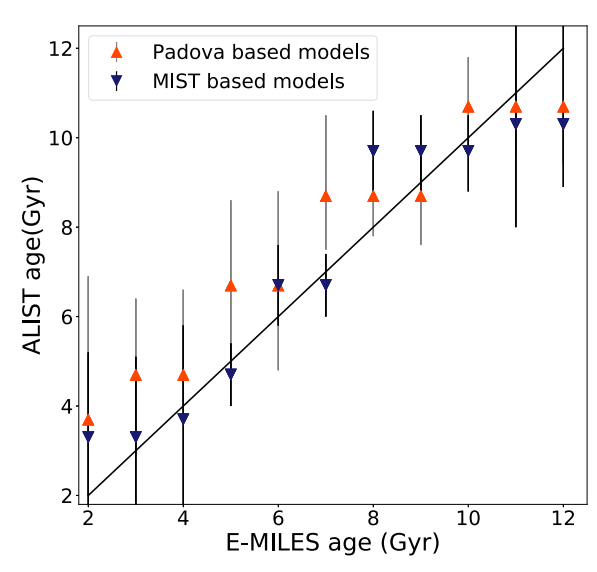
| | I | RV | | σ | [M | I/H] | α/M] | | |
|---------------------------|-----------------------|--------------|------------|---------------------|------------|--------------|--------------|--------------|--|
| | (km s ⁻¹) | | (kn | n s ⁻¹) | (dex) | | dex | | |
| | MIST-based | Padova-based | MIST-based | Padova-based | MIST-based | Padova-based | MIST-based | Padova-based | |
| Median offset | -1.5 | -1.3 | 0.4 | 0.2 | 0.04 | 0.09 | 0.02 | 0.02 | |
| Median absolute deviation | 0.74 | 0.66 | 1.55 | 1.53 | 0.08 | 0.1 | 0.04 | 0.04 | |

lower metallicity is consistent with the deeper lines seen for the same population parameters in the Padova-based templates relative to the MIST-based templates, due to the cooler AGB stars and luminosity-weighted $T_{\rm eff}$. A Spearman rank correlation between our A-LIST [α/M] values, and the [Mg/Fe] of Schiavon et al. (2012) gives a correlation coefficient of 0.64

and a *p*-value of 1.37×10^{-4} , suggesting a very significant correlation.

5.3. E-MILES Comparison

We also compare our library to the popular E-MILES (Vazdekis et al. 2016) models for the same age and metallicity.



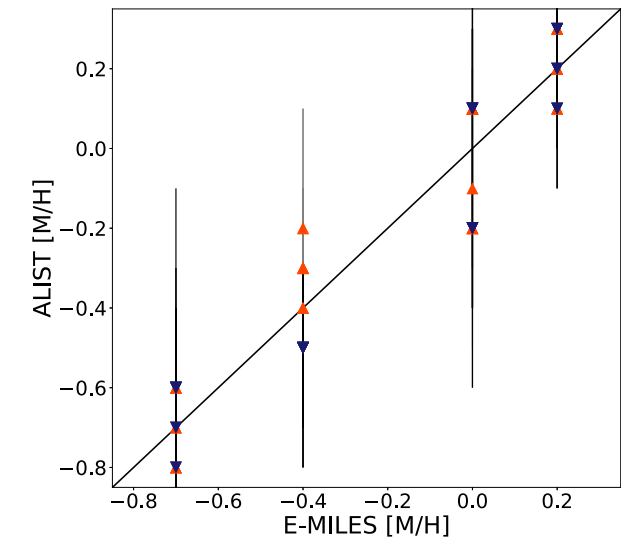


Figure 13. Age and [M/H] of best-fit low-resolution A-LIST models based on Padova (orange points) and MIST (blue points) isochrones compared with the E-MILES age and [Fe/H]. The uncertainties calculated are explained in Section 5.2.

The lower-metallicity E-MILES models (i.e., [Fe/H] < -0.4) are composite spectra generated by extrapolating the available SSP spectra from MIUSCAT (Vazdekis et al. 2012) and the IRTF library (Section 2 of Vazdekis et al. (2012)). Because our spectral resolution is much higher than that of E-MILES, we convolve the A-LIST spectra with a Gaussian kernel to reduce our resolution to match that of the E-MILES spectra. Using the pPXF code and the same fitting method as Section 5.2, we calculate the likelihood-weighted average values for the age and metallicity. The uncertainty or the "pseudo-error" on the A-LIST best-fit model is calculated using the same method as explained for the metallicity and α abundance in Section 5.2. Because these models do not have any errors on them, the pseudo-error is scaled by a normalized error (scatter between the best-fit model and the data) on the best-fit model.

Figure 13 shows the computed age and [M/H] from the best-fit reduced resolution Padova-based (orange) and MIST-based (blue) A-LIST templates (with $[\alpha/M] = 0$) fitted to E-MILES models at a range of ages (2–12 Gyr) and metallicities (–0.7, –0.4, –0.2, 0.0, and +0.2 dex).

Our models show close correspondence in both age and metallicity with lower-resolution E-MILES models. For Padova-based values (MIST-based values in parentheses), we find a median offset (E-MILES—A-LIST) of 0.7 (0.5) Gyr in age and 0.06 (0.06) dex in metallicity, while the median absolute deviation is 1.48 (0.88) Gyr in age and 0.09 (0.17) in metallicity. For the age comparison, MIST-based fits better match the E-MILES models, with both smaller offsets and a smaller median absolute deviation than the Padova-based fits. For metallicities, the two models provide quite similar offsets.

Figure 14 shows comparisons between the best-fit Padova-based A-LIST templates (at the E-MILES resolution; fuchsia) and E-MILES models (blue) using templates with solar α and a range of ages and metallicities. The differences between the best-fit Padova-based A-LIST and E-MILES models are shown in green.

5.4. Model Spectra Quality Test based on Globular Cluster Fitting

Two major factors affecting the reliability of the A-LIST model spectra, in terms of how representative a spectrum is of

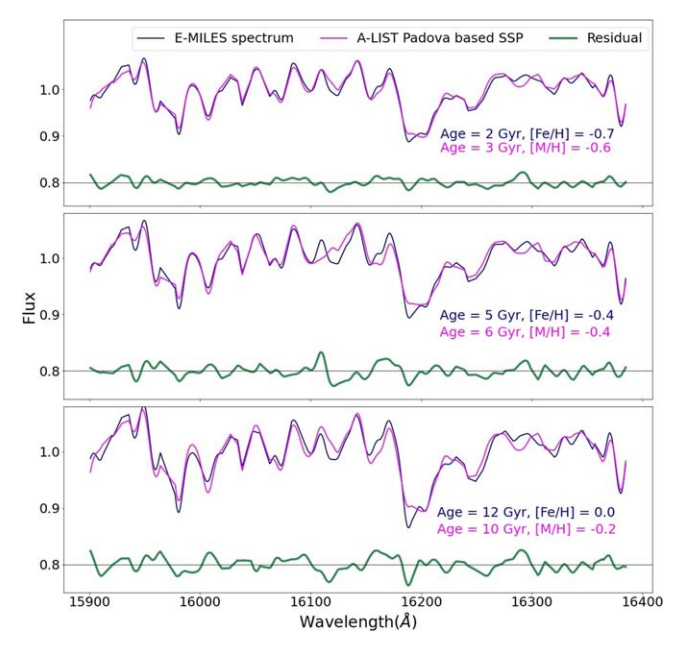


Figure 14. The best-fit Padova-based A-LIST templates (at reduced resolution, shown in fuchsia) compared with E-MILES spectra (shown in blue) at a range of ages and metallicities (with solar $[\alpha/M]$). The E-MILES age and metallicities are given in each panel in blue, and the best-fitting A-LIST template values in fuchsia. The differences between the spectra (A-LIST—E-MILES) are shown in green. The differences in the best-fit values between the Padova-based and MIST-based values for these models are small. The fits (Section 5.3) are performed over the full APOGEE wavelength range, but only a small section is shown here to highlight the similarity.

its nominal SSP, are the fraction of recovered luminosity (Section 4.1.1) and the difference in the luminosity-weighted average $T_{\rm eff}$ between the synthetic population and the model spectrum ($\Delta T_{\rm eff}$; Section 4.1.2). To understand how these affect our spectral models, we conduct tests in which we generate sets of modified A-LIST templates from a high luminosity fraction, low- $\Delta T_{\rm eff}$ model to simulate lower luminosity fractions and higher $\Delta T_{\rm eff}$ values (e.g., Figure 7). To test the effects of lower fractional luminosities, we remove the bins that have the largest contributions to the total SSP

luminosity. To test the effects of having a nonzero $\Delta T_{\rm eff}$, we remove the hottest and coldest $T_{\rm eff}$ bins.

For the recovered luminosity fraction test, we generate these degraded template sets for the best-fitting SSP to three of our high-S/N GCs (B127-G185, B151-G205, and B103-G165, with S/Ns of 150, 127, and 103, respectively). We perform the same fitting as in Section 5.1 and observe the relation between the χ^2 of the fits and the fractional luminosity. As the fractional luminosity decreases (i.e., the more bins we remove from the H-R diagram), the χ^2 values of the fits increase, as expected. Based on this increase in χ^2 , we define a cutoff fractional luminosity for the A-LIST models of 0.32, below which we caution the models may not provide reliable results. This value of 0.32 is selected based on where we see an increase in the reduced χ^2 of \sim 0.25 relative to the best-fit, highest luminosity fraction model.

We note that while this fraction may seem fairly low, many of the spectral bins in the HRD used in constructing our A-LIST models have spectra similar to each other, thus enabling accurate spectral models even at lower fractional luminosities.

We use two approaches for the $\Delta T_{\rm eff}$ test. In one, we generate degraded templates to fit the same three high-S/N GCs as above. To test how our models fare at different ages and metallicities, we also create mock data at younger ages and different metallicities by generating noisy data from our models assuming an S/N of 50. We then fit both the GCs and mock data to the degraded models using the same fitting method in Section 5.1 and observe the relation between the χ^2 of the fits and $\Delta T_{\rm eff}$. By progressively removing the hottest and coldest $T_{\rm eff}$ bins and then fitting the degraded templates to GC spectra or mock data created from our original models, we find that a $\Delta T_{\rm eff}$ of \sim -200 K and a $\Delta T_{\rm eff}$ of \sim +350 K correspond to a $\Delta \chi^2 \sim$ 0.25.

To summarize, we recommend using only models with luminosity fraction >0.32 and $-200~\mathrm{K} \leqslant \Delta T_{\mathrm{eff}} \leqslant 350~\mathrm{K}$; models meeting these requirements have been highlighted in Figure 8. Our "best" models (by these metrics) lie in the region of chemical space where the majority of Milky Way stars reside (the right panel of Figure 2). The quality of our models decreases in bins with few stars available (e.g., regions outside the white line in Figure 8(a)).

6. Summary

In this paper, we present A-LIST: a new spectral library of high-resolution, NIR integrated light SSP spectral templates that can be used to compute the properties of complex stellar populations having multiple populations with different ages, [M/H], and [α /M]. This library is generated using the isochrone synthesis method with Padova and MIST isochrones and a Kroupa (2001) IMF. We use an empirical stellar library with \sim 300,000 stars from the APOGEE survey, which has a spectral resolution of \sim 22,500 and a wavelength range of 15100 to 17000 Å. The empirical stellar library provides enough APOGEE spectra to generate SSP spectral models representing as much as 99% of the luminosity of the SSPs, with lower fractional luminosities found in regions of [M/H] and [α /M] space that are not well represented in the Milky Way.

Our validation tests demonstrate that our models give fitting results consistent in both age and metallicity with previous measurements and with lower-resolution models. First, we fit the A-LIST models to APOGEE spectra of M31 GCs and find metallicities consistent with previous measurements by Caldwell et al. (2011) and Sakari et al. (2016), with a median offset of <0.1 dex. The [α /M] measurements of our M31 GCs

are also well correlated with previously estimated values. Second, we fit our A-LIST library to E-MILES models at a range of ages and metallicities and find good agreement with the E-MILES models in the best-fit ages (with a median absolute deviation <1.5 Gyr) as well as the best-fit metallicities (with a median absolute deviation <0.17 dex).

We also use the fits to the globular clusters and to generated mock data to better understand where our models are most reliable. We find that models with fractional luminosity $\gtrsim\!0.32$, and with the difference in temperature between the synthetic population and our corresponding model of $-200~{\rm K} \leqslant \Delta T_{\rm eff} \leqslant 350~{\rm K}$, provide high-quality fits to the spectra. We recommend these thresholds in using our model spectra.

Our models are publicly available at https://github.com/aishashok/ALIST-library. We expect they will be useful in analyzing medium- and high-resolution *H*-band integrated light spectroscopy of galaxies and star clusters.

We would like to thank Ricardo Schiavon and Nelson Caldwell for providing us with the [Mg/Fe] abundances of M31 GCs. We would also like to thank the anonymous referee whose comments significantly improved this paper. Work on this project by A.A., G.Z., and A.S. was supported by NSF grant AST-1911129. Additional work was supported by NSF PHY-REU Award #1659494. D.A.G.H. acknowledges support from the State Research Agency (AEI) of the Spanish Ministry of Science, Innovation and Universities (MCIU) and the European Regional Development Fund (FEDER) under grant AYA2017-88254-P.

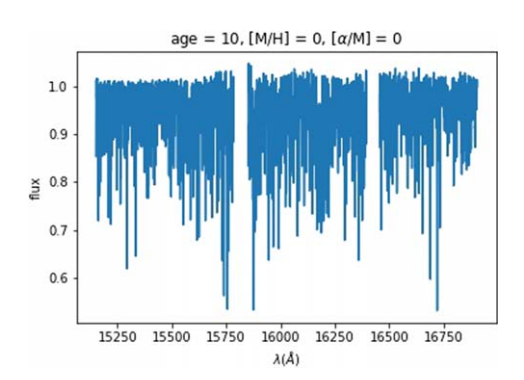
Funding for the Sloan Digital Sky Survey IV has been provided by the Alfred P. Sloan Foundation, the US Department of Energy Office of Science, and the Participating Institutions. SDSS-IV acknowledges support and resources from the Center for High-Performance Computing at the University of Utah. The SDSS website is www.sdss.org.

SDSS-IV is managed by the Astrophysical Research Consortium for the Participating Institutions of the SDSS Collaboration including the Brazilian Participation Group, the Carnegie Institution for Science, Carnegie Mellon University, the Chilean Participation Group, the French Participation Group, Harvard-Smithsonian Center for Astrophysics, Instituto de Astrofísica de Canarias, The Johns Hopkins University, Kavli Institute for the Physics and Mathematics of the Universe (IPMU)/University of Tokyo, the Korean Participation Group, Lawrence Berkeley National Laboratory, Leibniz Institut für Astrophysik Potsdam (AIP), Max-Planck-Institut für Astronomie (MPIA Heidelberg), Max-Planck-Institut für Astrophysik (MPA Garching), Max-Planck-Institut für Extraterrestrische Physik (MPE), National Astronomical Observatories of China, New Mexico State University, New York University, University of Notre Dame, Observatário Nacional/MCTI, The Ohio State University, Pennsylvania State University, Shanghai Astronomical Observatory, United Kingdom Participation Group, Universidad Nacional Autónoma de México, University of Arizona, University of Colorado Boulder, University of Oxford, University of Portsmouth, University of Utah, University of Virginia, University of Washington, University of Wisconsin, Vanderbilt University, and Yale University.

Appendix Sample Code to Access A-LIST Models

In this appendix, we present a sample code written in Python that can be used to read in the A-LIST models. For more detailed information about the contents of the models and how

```
import numpy as np #(version: 1.18.1)
import matplotlib.pyplot as plt #(version: 2.1.0)
3 from astropy.table import Table, Column #(version: 4.0.1.post1)
4 from astropy.io import fits #(version: 4.0.1.post1)
6 #Reading the .fits file to access the age, [M/H] and [$\alpha$/M] as well as the spectral models.
  #Here we are using astropy package in python.
s sspgrid = Table.read('A-LIST_padova.fits') #Contains the table with age, [M/H] and [$\alpha$/M]
9 ssp_spec = fits.open('A-LIST_padova.fits')[2].data # contains the spectral models
10 ssp_spec_uncert = fits.open('ALIST_Padova_variance.fits')[2].data #contains the variance spectra for each
##Selecting the models based on the quality cuts:
ixs_quality = np.where((sspgrid['lumfrac'] > 0.32) & (sspgrid['deltatemp'] > -200) &
       (sspgrid['deltatemp'] < 350))[0]</pre>
14
_{15} ##Define the age, [M/H] and [$\alpha$/M] needed to read-in:
16 age, m_h, a_m = 10, 0.0, 0.0
17 ##Pulling out a spectrum using the age, [M/H] and [$\alpha$/M] values from the table:
  model_id = np.where((sspgrid[ixs_quality]['AGE'] == age) & (sspgrid[ixs_quality]['M_H'] == m_h) & \
18
                      (sspgrid[ixs_quality]['A_M'] == a_m))[0]
  model_spec = ssp_spec[ixs_quality][model_id][0]
20
22 ##Defining the wavelength range using the information provided in the header.
  wavstart = float(fits.getheader('A-LIST_Padova.fits')['CRVAL1'].split()[0]) ##Starting wavelength in log
23
wavdelt = float(fits.getheader('A-LIST_Padova.fits')['CDELT1'].split()[0]) ##Delta wavelength in log space
25 numpix = int(fits.getheader('A-LIST_Padova.fits')['NWAVE'].split()[0]) ##Total number of pixels available
      in the spectra
  wavend = wavstart + (wavdelt*numpix) ##The wavelength value for the last pixel
  ##Using the information avilable above, we create an array of wavelength in the linear space using
      numpy's linspace:
  wavelength = 10**(np.linspace(wavstart, wavend, num = numpix))
29
31
32 ##An example plot to show what the spectrum looks like:
plt.plot(wavelength, model_spec)
34 ##These lines below are just the aesthetics of the plot.
plt.xlabel(r'$\lambda$($\AA$)')
36 plt.ylabel('flux')
37 plt.title(r'age = %d, [M/H] = %d, [$\alpha$/M] = %d'%(sspgrid['AGE'][model_id],
       sspgrid['M_H'][model_id],sspgrid['A_M'][model_id]))
38 plt.show()
```



to access them, please refer to the GitHub page: https://github.com/aishashok/ALIST-library.

ORCID iDs

Aishwarya Ashok https://orcid.org/0000-0003-1143-8502 Gail Zasowski https://orcid.org/0000-0001-6761-9359

Anil Seth https://orcid.org/0000-0003-0248-5470
Sten Hasselquist https://orcid.org/0000-0001-5388-0994
Dmitry Bizyaev https://orcid.org/0000-0002-3601-133X
D. A. García-Hernández https://orcid.org/0000-0002-1693-2721

Alexandre Roman-Lopes https://orcid.org/0000-0002-1379-4204

References

```
Ahumada, R., Allende Prieto, C., Almeida, A., et al. 2020, ApJS, 249, 3
Baldwin, C., McDermid, R. M., Kuntschner, H., Maraston, C., & Conroy, C.
  2018, MNRAS, 473, 4698
Beerman, L. C., Johnson, L. C., Fouesneau, M., et al. 2012, ApJ, 760, 104
Blanton, M. R., Bershady, M. A., Abolfathi, B., et al. 2017, AJ, 154, 28
Boardman, N., Zasowski, G., Seth, A., et al. 2020, MNRAS, 491, 3672
Böker, T., van der Marel, R. P., & Vacca, W. D. 1999, AJ, 118, 831
Bowen, I. S., & Vaughan, A. H. 1973, ApOpt, 12, 1430
Bressan, A., Marigo, P., Girardi, L., et al. 2012, MNRAS, 427, 127
Bruzual, G., & Charlot, S. 2003, MNRAS, 344, 1000
Caldwell, N., Schiavon, R., Morrison, H., Rose, J. A., & Harding, P. 2011, AJ,
   141.61
Cappellari, M. 2017, MNRAS, 466, 798
Cappellari, M., di Serego Alighieri, S., Cimatti, A., et al. 2009, ApJL, 704, L34
Cenarro, A. J., Cardiel, N., Gorgas, J., et al. 2001, MNRAS, 326, 959
Cenarro, A. J., Cardiel, N., Vazdekis, A., & Gorgas, J. 2009, MNRAS,
  396, 1895
Cesetti, M., Ivanov, V. D., Morelli, L., et al. 2009, A&A, 497, 41
Chavez, M., Malagnini, M. L., & Morossi, C. 1996, ApJ, 471, 726
Chen, Y., Bressan, A., Girardi, L., et al. 2015, MNRAS, 452, 1068
Chen, Y., Girardi, L., Bressan, A., et al. 2014, MNRAS, 444, 2525
Choi, J., Dotter, A., Conroy, C., et al. 2016, ApJ, 823, 102
Cid Fernandes, R., Mateus, A., Sodré, L., Stasinska, G., & Gomes, J. M. 2011,
   STARLIGHT: Spectral Synthesis Code, Astrophysics Source Code Library,
   ascl:1108.006
Cignoni, M., Sacchi, E., Tosi, M., et al. 2019, ApJ, 887, 112
Cirasuolo, M. 2016, in ASP Conf. Ser., 507, MOONS: A New Powerful Multi-
   Object Spectrograph for the VLT, ed. I. Skillen, M. Balcells, & S. Trager
   (San Francisco, CA: ASP), 109
Coelho, P. R. T., Bruzual, G., & Charlot, S. 2020, MNRAS, 491, 2025
Conroy, C. 2013, ARA&A, 51, 393
Conroy, C., Villaume, A., van Dokkum, P. G., & Lind, K. 2018, ApJ, 854, 139
Cushing, M. C., Rayner, J. T., & Vacca, W. D. 2005, ApJ, 623, 1115
Dahmer-Hahn, L. G., Riffel, R., Rodríguez-Ardila, A., et al. 2018, MNRAS,
  476, 4459
De Silva, G. M., Freeman, K. C., Bland-Hawthorn, J., et al. 2015, MNRAS,
   449, 2604
Dotter, A. 2016, ApJS, 222, 8
Durbin, M. J., Beaton, R. L., Dalcanton, J. J., Williams, B. F., & Boyer, M. L.
   2020, ApJ, 898, 57
Eisenhauer, F., Abuter, R., Bickert, K., et al. 2003, Proc. SPIE, 4841, 1548
Eisenstein, D. J., Weinberg, D. H., Agol, E., et al. 2011, AJ, 142, 72
Elias, J. H., Joyce, R. R., Liang, M., et al. 2006, Proc. SPIE, 6269, 62694C
Förster Schreiber, N. M., Genzel, R., Lutz, D., & Sternberg, A. 2003, ApJ,
   599, 193
Gallazzi, A., Charlot, S., Brinchmann, J., White, S. D. M., & Tremonti, C. A.
   2005, MNRAS, 362, 41
García Pérez, A. E., Allende Prieto, C., Holtzman, J. A., et al. 2016, AJ,
   151, 144
Gonneau, A., Lyubenova, M., Lançon, A., et al. 2020, A&A, 634, A133
Gratton, R. G., Carretta, E., & Bragaglia, A. 2012, A&ARv, 20, 50
Gunn, J. E., Siegmund, W. A., Mannery, E. J., et al. 2006, AJ, 131, 2332
Gustafsson, B., Edvardsson, B., Eriksson, K., et al. 2008, A&A, 486, 951
Heavens, A., Panter, B., Jimenez, R., & Dunlop, J. 2004, Natur, 428, 625
Holtzman, J. A., Hasselquist, S., Shetrone, M., et al. 2018, AJ, 156, 125
Hosek, M. W., Jr., Lu, J. R., Lam, C. Y., et al. 2020, AJ, 160, 143
Janz, J., Norris, M. A., Forbes, D. A., et al. 2016, MNRAS, 456, 617
Johnston, E. J., Puzia, T. H., D'Ago, G., et al. 2020, MNRAS, 495, 2247
Jönsson, H., Allende Prieto, C., Holtzman, J. A., et al. 2018, AJ, 156, 126
Jönsson, H., Holtzman, J. A., Prieto, C. A., et al. 2020, AJ, 160, 120
Koleva, M., Prugniel, P., Bouchard, A., & Wu, Y. 2009, A&A, 501, 1269
Kroupa, P. 2001, MNRAS, 322, 231
La Barbera, F., Vazdekis, A., Ferreras, I., et al. 2016, MNRAS, 457, 1468
La Barbera, F., Vazdekis, A., Ferreras, I., et al. 2017, MNRAS, 464, 3597
Leitherer, C., Ekström, S., Meynet, G., et al. 2014, ApJS, 212, 14
Leung, H. W., & Bovy, J. 2019, MNRAS, 483, 3255
Lewis, A. R., Dalcanton, J. J., Dolphin, A. E., Weisz, D. R., & Williams, B. F.
   2015, in IAU Symposium, Vol. 309, Galaxies in 3D across the Universe, ed.
   B. L. Ziegler et al. (Cambridge: Cambridge Univ. Press), 57
Lu, J. R., Do, T., Ghez, A. M., et al. 2013, ApJ, 764, 155
MacArthur, L. A., McDonald, M., Courteau, S., & Jesús González, J. 2010,
   ApJ, 718, 768
```

```
Mackereth, J. T., Bovy, J., Leung, H. W., et al. 2019, MNRAS, 489, 176
Majewski, S. R., Schiavon, R. P., Frinchaboy, P. M., et al. 2017, AJ, 154, 94
Maraston, C. 2005, MNRAS, 362, 799
Maraston, C., & Strömbäck, G. 2011, MNRAS, 418, 2785
Maraston, C., Strömbäck, G., Thomas, D., Wake, D. A., & Nichol, R. C. 2009,
   MNRAS, 394, L107
Marigo, P., Girardi, L., Bressan, A., et al. 2017, ApJ, 835, 77
Mármol-Queraltó, E., Cardiel, N., Cenarro, A. J., et al. 2008, A&A, 489, 885
Martins, L. P., Lima-Dias, C., Coelho, P. R. T., & Laganá, T. F. 2019,
    MNRAS, 484, 2388
McDermid, R. M., Alatalo, K., Blitz, L., et al. 2015, MNRAS, 448, 3484
McGregor, P. J., Hart, J., Conroy, P. G., et al. 2003, Proc. SPIE, 4841, 1581
Meneses-Goytia, S., Peletier, R. F., Trager, S. C., & Vazdekis, A. 2015, A&A,
  582, A97
Mould, J. R. 1978, ApJ, 220, 434
Nidever, D. L., Holtzman, J. A., Allende Prieto, C., et al. 2015, AJ, 150, 173
Ocvirk, P., Pichon, C., Lançon, A., & Thiébaut, E. 2006, MNRAS, 365, 46
Onken, C. A., Valluri, M., Brown, J. S., et al. 2014, ApJ, 791, 37
Pace, Z. J., Tremonti, C., Chen, Y., et al. 2019, ApJ, 883, 82
Parikh, T., Thomas, D., Maraston, C., et al. 2019, MNRAS, 483, 3420
Pastorelli, G., Marigo, P., Girardi, L., et al. 2019, MNRAS, 485, 5666
Paxton, B., Bildsten, L., Dotter, A., et al. 2011, ApJS, 192, 3
Paxton, B., Cantiello, M., Arras, P., et al. 2013, ApJS, 208, 4
Paxton, B., Marchant, P., Schwab, J., et al. 2015, ApJS, 220, 15
Pérez, E., Cid Fernandes, R., González Delgado, R. M., et al. 2013, ApJL,
  764, L1
Pickles, A. J. 1998, PASP, 110, 863
Prugniel, P., Soubiran, C., Koleva, M., & Le Borgne, D. 2007, arXiv:astro-ph/
  0703658
Rayner, J. T., Cushing, M. C., & Vacca, W. D. 2009, ApJS, 185, 289
Riffel, R., Rodríguez-Ardila, A., Brotherton, M. S., et al. 2019, MNRAS,
Röck, B., Vazdekis, A., La Barbera, F., et al. 2017, MNRAS, 472, 361
Röck, B., Vazdekis, A., Ricciardelli, E., et al. 2016, A&A, 589, A73
Ruiz-Lara, T., Gallart, C., Bernard, E. J., & Cassisi, S. 2020, NatAs, 4, 965
Sakari, C. M., Shetrone, M. D., Schiavon, R. P., et al. 2016, ApJ, 829, 116
Salaris, M., & Cassisi, S. 2005, Evolution of Stars and Stellar Populations
  (Weinheim: Wiley)
Sánchez, S. F., Pérez, E., Sánchez-Blázquez, P., et al. 2016a, RMxAA, 52, 21
Sánchez, S. F., Pérez, E., Sánchez-Blázquez, P., et al. 2016b, RMxAA, 52, 171
Schiavon, R. P. 2007, ApJS, 171, 146
Schiavon, R. P., Caldwell, N., Morrison, H., et al. 2012, AJ, 143, 14
Serenelli, A., Weiss, A., Cassisi, S., Salaris, M., & Pietrinferni, A. 2017, A&A,
  606, A33
Silva, D. R., Kuntschner, H., & Lyubenova, M. 2008, ApJ, 674, 194
Spinrad, H., & Taylor, B. J. 1971, ApJS, 22, 445
Steidel, C. C., Rudie, G. C., Strom, A. L., et al. 2014, ApJ, 795, 165
Strader, J., Caldwell, N., & Seth, A. C. 2011, AJ, 142, 8
Tang, J., Bressan, A., Rosenfield, P., et al. 2014, MNRAS, 445, 4287
Thomas, D., Maraston, C., & Bender, R. 2003, MNRAS, 339, 897
Tinsley, B. M. 1968, ApJ, 151, 547
Tojeiro, R. 2007, in ASP Conf. Ser., 374, From Stars to Galaxies: Building the
  Pieces to Build Up the Universe, ed. A. Vallenari et al. (San Francisco, CA:
  ASP), 507
Trager, S. C., Faber, S. M., Worthey, G., & González, J. J. 2000, AJ, 119, 1645
Vazdekis, A., Casuso, E., Peletier, R. F., & Beckman, J. E. 1996, ApJS,
  106, 307
Vazdekis, A., Koleva, M., Ricciardelli, E., Röck, B., & Falcón-Barroso, J.
  2016, MNRAS, 463, 3409
Vazdekis, A., Ricciardelli, E., Cenarro, A. J., et al. 2012, MNRAS, 424, 157
Vazdekis, A., Sánchez-Blázquez, P., Falcón-Barroso, J., et al. 2010, MNRAS,
  404, 1639
Weisz, D. R., Dolphin, A. E., Dalcanton, J. J., et al. 2011, ApJ, 743, 8
Wilkinson, D. M., Maraston, C., Goddard, D., Thomas, D., & Parikh, T. 2017,
    MNRAS, 472, 4297
Williams, B. F., Dalcanton, J. J., Seth, A. C., et al. 2009, AJ, 137, 419
Wilson, J. C., Hearty, F. R., Skrutskie, M. F., et al. 2019, PASP, 131, 055001
Wisnioski, E., Förster Schreiber, N. M., Wuyts, S., et al. 2015, ApJ, 799, 209
Worthey, G., Faber, S. M., Gonzalez, J. J., & Burstein, D. 1994, ApJS, 94, 687
Ygouf, M., Beichman, C., Hodapp, K., & Roellig, T. 2017, in SF2A-2017:
  Proc. Annual Meeting of the French Society of Astronomy and
  Astrophysics, ed. C. Reylé et al. (Paris: SF2A), 325
Zasowski, G., Cohen, R. E., Chojnowski, S. D., et al. 2017, AJ, 154, 198
Zasowski, G., Johnson, J. A., Frinchaboy, P. M., et al. 2013, AJ, 146, 81
```